First observation of a quadruple asteroid. Detection of a third moon around (130) Elektra with SPHERE/IFS

Anthony Berdeu, Maud Langlois, Frédéric Vachier

A&A 658, L4 (2022)
https://doi.org/10.1051/0004-6361/202142623

Astronomy & Astrophysics

LETTER TO THE EDITOR

First observation of a quadruple asteroid

Detection of a third moon around (130) Elektra with SPHERE/IFS⋆,⋆⋆

Anthony Berdeu[1,2], Maud Langlois[3], and Frédéric Vachier[4]

[1] National Astronomical Research Institute of Thailand, 260 Moo 4, T. Donkaew, A. Maerim, Chiang Mai 50180, Thailand
e-mail: anthony@narit.or.th
[2] Department of Physics, Faculty of Science, Chulalongkorn University, 254 Phayathai Road, Pathumwan, Bangkok 10330, Thailand
[3] Université de Lyon, Université Lyon1, ENS de Lyon, CNRS, Centre de Recherche Astrophysique de Lyon UMR 5574, 69230 Saint-Genis-Laval, France
[4] Institut de Mécanique Céleste et de Calcul des Ephémérides, CNRS, Observatoire de Paris, PSL Université, Sorbonne Université, Paris, France

Received 9 November 2021 / Accepted 6 January 2022

ABSTRACT

Context. Extreme adaptive optics systems, such as the Spectro-Polarimetric High-contrast Exoplanet REsearch facility (SPHERE), push forward the limits in high contrast and high resolution in direct imaging. The main objectives of these instruments are exoplanet detection and characterisation.
Aims. We aim to increase the contrast limits to detect new satellites orbiting known asteroids. We use cutting-edge data reduction techniques and data processing algorithms that are essential to best analyse the raw data provided by the instruments and increase their performances. Doing so, the unequalled performances of SPHERE also make it a unique tool to resolve and study asteroids in the solar system, expanding the domain of its main science targets.
Methods. We applied a newly developed data reduction pipeline for integral field spectrographs on archival SPHERE data of a resolved asteroid, (130) Elektra. It was coupled with a dedicated point spread function reconstruction algorithm to model the asteroid halo. Following the halo removal, the moon signal could be extracted more accurately. The moon positions were fitted at three epochs and were used to derive the orbital parameters via a genetic-based algorithm.
Results. We announce the discovery of S/2014 (130) 2, a third moon orbiting (130) Elektra, making it the first quadruple asteroid ever found. It is identified in three different epochs, 9, 30, and 31 Dec. 2014, at a respective angular separation of 258 mas (333 km), 229 mas (327 km), and 319 mas (457 km). We estimate that this moon has a period of 0.679 ± 0.001 day and a semi-major axis of 344 ± 5 km, with an eccentricity of 0.33 ± 0.05 and an inclination of 38° ± 19° compared to the primary rotation axis. With a relative magnitude to the primary of 10.5 ± 0.5, its size is estimated to be 1.6 ± 0.4 km.
Conclusions. The orbital parameters of S/2014 (130) 2 are poorly constrained due to the unfavourable configurations of the available fragmentary data. Additional observations are needed to better estimate its orbit and to suggest a formation model. This new detection nonetheless shows that dedicated data reduction and processing algorithms modelling the physics of the instruments can push their contrast limits further.

Key words. instrumentation: adaptive optics – instrumentation: high angular resolution – methods: numerical – techniques: high angular resolution – techniques: image processing – minor planets, asteroids: individual: (130) Elektra

1. Introduction

More than two decades ago, the advent of adaptive optics (AO) systems triggered a leap forward in the study of asteroids. The first satellite imaged, aside from a spacecraft flyby, was that of (45) Eugenia (Merline et al. 1999) using one of the first (classical) AO systems applied to asteroids (Probing the Universe with Enhanced Optics, PUEO, at the Canada-France-Hawaii Telescope). At the same time, other methods (see Merline et al. 2002, for a complete summary of the early methods) were also closing the gap to detect satellites: light curve methods, radar, *Hubble* Space Telescope imaging, and direct imaging without AO from the ground, and even occultations.

During the last decade, extreme AO (XAO) systems have pushed the instruments to even higher contrast and resolution (Jovanovic et al. 2015; Fusco et al. 2016). Such systems, developed for exoplanet research, are also being applied to asteroids (Marchis & Vega 2014). It is clear that these XAO systems will be required to get the best data on exoplanets and asteroids from existing and newer, larger telescopes.

High resolution. The Zurich Imaging Polarimeter instrument (ZIMPOL, Schmid et al. 2018) on the Spectro-Polarimetric High-contrast Exoplanet REsearch adaptive optics system and coronagraphic facility (SPHERE, Beuzit et al. 2019), on the Very Large Telescope (VLT), works in the visible band

⋆ Visualisations are available at https://www.aanda.org
⋆⋆ Based on publicly available archival data provided by the ESO Science Archive Facility under programme ID 60.A-9362(A) (Yang et al.).

(500 to 900 nm) and possesses an unequalled angular resolution. Resolving the asteroid surfaces paves the way to their topology analysis and their 3D shape estimation (Marchis et al. 2021; Vernazza et al. 2021). This gives access to their density and provides some hints as to their composition and origin.

High contrast. Reaching deeper contrasts naturally led to the detection of faint moons orbiting asteroids, such as in the system of (87) Sylvia, the first trinary asteroid, discovered by Marchis et al. (2005) with the NACO (NAOS – CONICA, Nasmyth Adaptive Optics System – Near-Infrared Imager and Spectrograph) instrument on the VLT. Resolving and monitoring moon systems are keys to probing the gravitational field of these complex objects and understanding their dynamics (see e.g., Berthier et al. 2014; Pajuelo et al. 2018; Carry et al. 2021; Marchis et al. 2021).

In addition to ZIMPOL, SPHERE is also equipped with an integral field spectrograph (IFS, Claudi et al. 2008) and the InfraRed Dual-band Imager and Spectrograph (IRDIS, Dohlen et al. 2008) working in near-infrared bands (NIR). The primary goals of these instruments are the imaging and the characterisation of exoplanets by achieving higher contrasts via the use of a coronagraphic mask (Vigan et al. 2021). However, these instruments can also be used for the observation of extended objects (see e.g., Hanus et al. 2017; King et al. 2019; Souami et al. 2022). Their better AO and contrast performances at these longer wavelengths compared to ZIMPOL also make them very efficient for the detection of faint moons orbiting close to a bright primary such as the second moon of (107) Camilla, discovered by Marsset et al. (2016) in IFS data.

Along with this new instrumentation, new data reduction techniques must keep pace. In this Letter, we apply our newly developed reduction pipeline for SPHERE/IFS, PIC (Projection, Interpolation, Convolution, Berdeu et al. 2020) on an archival dataset of asteroid (130) Elektra (hereafter Elektra). By correcting the artefacts of the SPHERE Data Centre pipeline (SPHERE/DC, Delorme et al. 2017), PIC strongly improves the quality of the data reductions. After the careful removal of the asteroid halo with our new dedicated point spread function (PSF) reconstruction algorithm, we discovered and extracted a new satellite orbiting Elektra, making it the third satellite in this system, designated as S/2014 (130) 2 (hereafter S3). Its first satellite, S/2003 (130) 1 (hereafter S1), was discovered by Merline et al. (2003) using the Keck AO system and its second satellite, S/2014 (130) 1 (hereafter S2), was discovered by Yang et al. (2016) jointly in IFS and IRDIS data, in the same dataset that we use in this Letter.

Elektra is the first quadruple system ever detected. A preliminary dynamical study is performed on these fragmentary data to confirm that this detection is not an artefact. Additional observations are needed to better constrain the orbit of S3 and propose a formation model.

2. SPHERE/IFS observation and data reduction

Elektra was observed on 6 Dec. 2014 and 9 Dec. 2014 as part of the SPHERE science verification program by Yang et al. (60.A-9362(A) – 'Origin of Multiple Asteroid Systems by Component-Resolved Spectroscopy'). They obtained additional observations on 30 Dec. 2014 and 31 Dec. 2014, using director's discretionary time (Yang et al. 2016). These data were acquired using the IFS of SPHERE via its YJH filter (0.95 to 1.65 µm). We retrieved these publicly available datasets from the European Southern Observatory (ESO) archives. Nonetheless, we could not find the IFS data of 6 Dec. 2014 and they are consequently not presented in this Letter[1].

The raw data were reduced using the PIC pipeline (Berdeu et al. 2020). The reduction is based on an inverse problem approach solved via a robust penalisation with spectral and spatial regularisations. To show the relevance of the PIC pipeline, the dataset of 9 Dec. 2014 was also reduced with the SPHERE/DC (Delorme et al. 2017). The two pipelines are compared in detail in Appendix B.

We would like to mention here that data were simultaneously acquired with IRDIS (Yang et al. 2016), but they are highly noisy due to inappropriate detector integration time (DIT) selection and we consequently could not detect the presence of S3 in these datasets. As a consequence, they are not presented in this Letter.

3. Image processing: Overview

Angularly speaking, the two already known moons around Elektra revolve very closely to the asteroid and S2 is nearly buried in its halo (Yang et al. 2016). The detection of an even fainter and closer moon implies a careful estimate and removal of this halo.

For the detection of S2, Yang et al. (2016) straightforwardly adapted a technique described by Wahhaj et al. (2013). Initially developed for exoplanet detection to remove residual speckles in coronagraph images, it uses local medians on arcs centred on the primary, removed from each pixel. This technique does not account for the physics of the halo that is poorly estimated, and it can result in some self-subtraction that can bias the moon photometry or even prevent its detection.

To circumvent these effects, we present a halo removal technique here based on a physical model to describe its shape. The halo comes from the faint extensions, so-called wings, of the PSF that make the light of the asteroid scatter far from its photometric surface. In other words, the halo can be modelled by the convolution of the asteroid image with the wings of the instrument PSF. But the sharp image of the asteroid is unknown and the PSF cannot be predicted as it depends on the seeing conditions and the AO performances during each acquisition. As a consequence, these two components of the model must be estimated jointly and directly from the data, a problem known as blind deconvolution (Lam & Goodman 2000; Mugnier et al. 2004; Soulez et al. 2012).

Thus, along with the object deconvolution, one objective of the algorithm is to reconstruct the AO-corrected PSF of each reduced hypercube. Our PSF model is based on the sum of two components: its core and its wings. It is similar to what has been proposed by Fétick et al. (2019) where the PSF is modelled by the convolution of the diffraction-limited PSF of the instrument (shaping its core) by the PSF of the atmosphere fitted with a modified two-dimensional (2D) Moffat function (shaping its wings). The steps of Algorithm 1 are detailed in Appendix A and summarised in Fig. 1. In short, the core of the PSF was fitted on the brightest moon, see Fig. A.1a. By deconvolving the reduced image (Fig. 1a,c), with this PSF, a sharp image of the primary was obtained, see Fig. 1b. This sharp image was used to fit the PSF wings and produce a halo model (Fig. 1d). This model was then removed from the data (Fig. 1e), that is to say further cleaned with a median filter (Fig. 1f), to reveal faint objects in the primary vicinity.

[1] On this matter, we contacted the ESO data archive facility that could not recover this dataset. At the time of submission, it seems that this IFS dataset is unavailable.

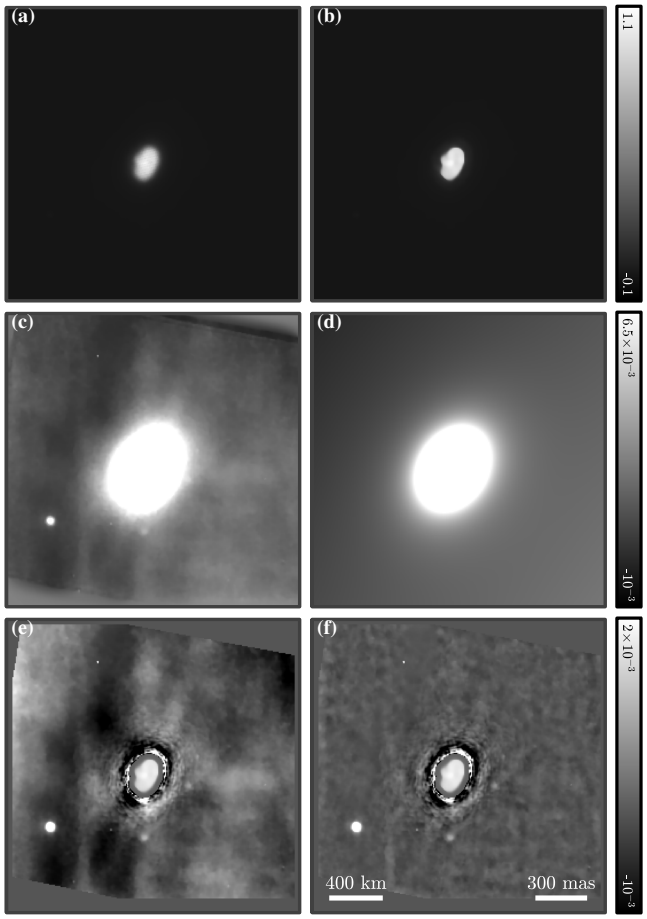

Fig. 1. Overview of the image processing steps, applied on the 24th acquisition of 9 Dec. 2014 after its reduction by PIC (Berdeu et al. 2020). (a) Normalised reduced data. (b) Deconvolved object. (c) Saturated view of (a). (d) Saturated view of the fitted halo model. (e) Residuals after the subtraction from (a,c) of the halo model (d). (f) Residuals after the application of the annulus median filter on (e). In (e) and (f), the unusable pixels for the halo fitting and the median filtering (edges of the IFS field-of-view and deconvolved primary) have been replaced by a dimmer view of (b) to simultaneously visualise the primary and the moons.

The scale bars of Fig. 1 emphasise the importance of the halo removal. Indeed, the intensity on the newly discovered moon in Fig. 1f is ∼1500 fainter than the primary surface intensity (7×10^{-4}), while the halo is only ∼150 fainter (6×10^{-3}) in Figs. 1a,c.

4. Satellites' relative astrometry and photometry

After the image processing described in the previous section, the different frames were centred on the photocentre of Elektra by computing the centroid of its segmented deconvolved reconstruction and orientated towards the north using calibrations from Maire et al. (2021). The temporal median projections of each sequence are given in Fig. 2. The three moons are clearly visible at all epochs.

To extract the astrophotometry of the three satellites, we used MPFIT2DPEAK[2], a 2D non-linear least squares Gaussian fitter. It returns the peak intensity, half-widths (independent semi-major and semi-minor axes), and position of each moon for each image of the observation sequences. We included a rejection criteria based on the full-width at half-maximum if greater or smaller by 60% from the median (25 mas). To account for the satellite motion and to reduce astrometric uncertainty, we refined the astrometry with a temporal linear fit on the polar positions for each epoch, see Fig. B.4. Visualisations 1, 2, and 3[3] show the time-lapses of the linearly fitted positions at the different epochs. The astrophotometry fits on the three moons are listed in the tables of Appendix E. On average, S3 was found in the three different epochs (9, 30 , and 31 Dec. 2014) at a respective angular separation of 258 mas (333 km), 229 mas (327 km), and 319 mas (457 km) from Elektra.

For the pixel scale of the SPHERE/DC pipeline, we used a constant value of 7.46 ± 0.02 mas pixel^{-1} (Maire et al. 2021). It corresponds to a pixel scale of 6.66 ± 0.02 mas pixel^{-1} for the reductions with PIC (Berdeu et al. 2020). The true north (TN) correction of $-1.75°$ typically has an error of $\pm0.07°$ (Maire et al. 2021). This TN error includes the observed systematic error in the parallactic angle estimation due to backlash in the derotator mechanism (∼0.05°), as reported by Beuzit et al. (2019). For the IFS, an additional offset of 100.48° in the clockwise direction was applied to account for the orientation of the instrument's field of view. The astrometric errors were estimated by including the following systematics described by Langlois et al. (2021) and Maire et al. (2021): plate scale and TN errors, the error on the satellite centring (estimated from the standard deviation from the linear fit), and the error on the primary centring. The accurate timestamps were computed from the data `fits` header for each DIT by including a parametric model of the overheads occurring during the data recording (Delorme et al. 2017).

The relative photometry between Elektra and S1 was obtained with the ratio of their integrated flux. The integrated flux of Elektra was calculated by integrating its segmented deconvolved reconstruction. By definition, this measurement does not account for the energy ratio diluted in the halo and attributable to the wing of the PSF. The integrated flux of the brightest moon S1 was obtained by integrating the 2D Gaussian function fitted for the PSF core fitting (see Appendix A.1). Once again, this does not account for the ratio of the flux in the PSF wing (see Fig. A.2c). These techniques make the two measurements coherent and conserve their intensity ratio. The relative photometry between the three moons was obtained by scaling the ratio of their Gaussian amplitude fitted as described above. Based on these measurements, the mean magnitude difference through the YJH band (0.95–1.65 µm) between Elektra and its companions is 7.6 ± 0.2 for S1, 10.0 ± 0.4 for S2, and 10.5 ± 0.5 for S3 based on the 9 Dec. 2014 observation (see Appendix E).

Assuming that the moons have the same albedo as the primary, it is possible to estimate their diameter from these relative magnitude. Taking 199 ± 7 km as the effective diameter for Elektra (Hanus et al. 2017; Miles et al. 2018), S1 is 6.0 ± 0.6 km, S2 is 2.0 ± 0.4 km, and S3 is 1.6 ± 0.4 km. Our estimates on S1 and S2 are in agreement with the values announced by Yang et al. (2016) of 6.0 ± 1.5 km and 2.0 ± 1.5 km, respectively. In addition, the size of S1 was estimated to be 4 km by Merline et al. (2003) and 7 km by Marchis et al. (2008).

5. Orbital fitting

The gravitational environment, in which S3 evolves, is dominated by the zonal coefficient J_2 (Yang et al. 2016). The

[2] Craig B. Markwardt, NASA/GSFC Code 662, Greenbelt, MD 20770, http://cow.physics.wisc.edu/~craigm/idl/idl.html

[3] https://www.aanda.org/10.1051/0004-6361/202142623/olm

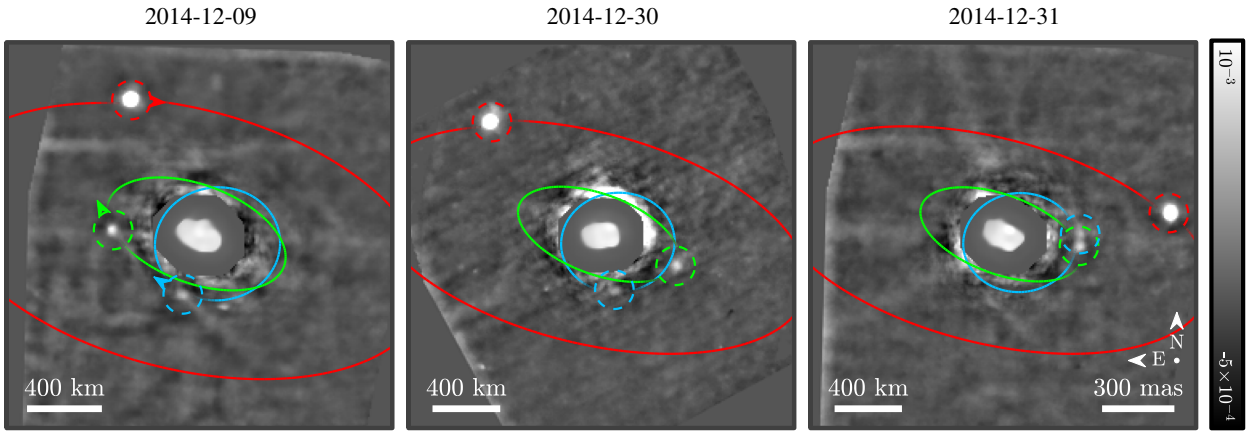

Fig. 2. Median projection of the temporal cubes for the different dates reduced with the PIC pipeline (Berdeu et al. 2020). The fitted orbits are projected on the different dates: S1 in red, S2 in green, and S3 in blue. The arrows indicate the projected motion direction. The dashed circles indicate the median fitted moon position during the acquisitions at each date. The central part of the field of view has been replaced by a dimmer deconvolved image of Elektra to simultaneously visualise the primary and the moons.

observations of S3 that we measured are separated only by 3 weeks, which represents about 33 revolutions. This is sufficient for the satellite to be disturbed by the J_2. However, the position of S3 in the observations are all located on the same side of the orbit, as is visible in Fig. 2. Thus, the distribution of the observations is fragmentary, both spatially and temporally. This is an unfavourable situation in which to constrain the orbit parameters. Moreover, taking the J_2 into account is certainly insufficient to describe the gravitational field generated by Elektra over a long period of time.

As a consequence, we fitted Keplerian orbits for the three moons ($J_2 = 0$), centred on Elektra's photocentre. Such Keplerian model is generally more robust and stable in such a situation (Yang et al. 2016).

We used the Genoid algorithm (GENetic Orbit IDentification, Vachier et al. 2012; Berthier et al. 2014; Pajuelo et al. 2018; Carry et al. 2019) to fit the Keplerian model to the observations. It is a genetic-based algorithm that relies on a metaheuristic method to find the best-fit (i.e. minimum χ^2) set of dynamical parameters (among others: mass M, period P, semi-major axis a, eccentricity e, inclination i, longitude of the node Ω, argument of pericentre ω, and time of passage to pericentre t_p) by refining, generation after generation, a grid of test values.

For a purely Keplerian fit, the unknowns driving the system dynamics are the system mass and the six independent orbital parameters of each moon listed above (M, P, and a are linked according to Kepler's second law). Standard detection techniques combine the frames in each epoch to increase the signal-to-noise ratio, for example by averaging the frames or taking their median. This leads to only two data points per night (x and y positions), and thus here six points in total for each moon. This would make the system under-constrained, missing one independent measurement. With our method, the efficiency of the halo removal allows one to fit the astrometry of the moons in almost each frame of the different epochs. Combined with the robustness of the linear fit, it is then possible to fit a small arc of the orbit in each dataset (see Fig. B.4). If all these measurements are not independent, they at least give access to the local derivatives of each moon orbit, increasing the number of data points per night to four (x and y positions and their derivatives). These derivatives help Genoid to reject orbits passing through the data points, but with the wrong local tangent. It is then possible to fit all the parameters of the Keplerian model. Nonetheless, some parameters will still be poorly constrained, as shown below.

As detailed in Appendix C.1, additional archival data on S1 are available, ranging from 2003 to 2019. These data are used to estimate a first guess on the system mass and S1's orbital parameters. This guess is used to initialise the Genoid fit on the 2014 datasets where Elektra's mass and the orbital parameters of the three moons are then let free to evolve. As further discussed in Appendix C.1, the evolution of the viewing angle on the system between 6 Dec. and 31 Dec., combined with the knowledge of the local arcs of the orbits with a good astrometry precision, are sufficient for Genoid to favour one orbital pole solution of its different degenerate symmetries. We present this solution in the following.

This global fit provides an overall root mean square (RMS) error of 6.8 mas between the positions predicted by the model and the astrometry measurements. This error is in good agreement with the uncertainties on the astrometry, listed in Appendix E. The fit RMS error per moon is 3.5 mas for S1, 2.4 mas for S2, and 11.3 mas for S3. This last value can suggest that a Keplerian fit is only a first order approximation. It is also consistent with the fact that despite the halo removal, the residuals are still high and possibly corrupt the astrometry fit, as shown by the dispersion of the measurements in Fig. B.4.

Elektra's estimated derived mass is $(7.0 \pm 0.3) \times 10^{18}$ kg. The orbital elements of S3 are given in Table 1. These values should be considered with great precaution. The orbit seems very eccentric ($e = 0.33 \pm 0.05$) and inclined with respect to the spin axis of Elektra ($38° \pm 19°$), as shown in Table C.4. Also, the orbital elements of S1 and S2 are listed in Appendix C.2.

Figure 2 shows the orbits of the different satellites. S3 is highlighted in blue. For the observation of 31 Dec. 2014, we can see a close projected approach of S3 with S2, at more than 400 km from Elektra. This emphasises the high eccentricity of the orbit.

In Appendix D, we present some hints for the presence of S3 in other datasets obtained with the IFS in 2016 and ZIMPOL in 2019. They are nonetheless temporally too far from the 2014 observations to be included in the orbit fitting presented in this section. Taking them into account requires substantial work that is beyond the scope of this Letter.

Table 1. Orbital elements of S3 expressed in EQJ2000.

S3 – S/2014 (130) 2		
Observing data set		
Number of observations	120	
Time span (days)	22	
RMS (mas)	11.31	
Orbital elements EQJ2000		
P (day)	0.679	±0.001
a (km)	344	±5
e	0.33	±0.05
i (°)	129	±24
Ω (°)	127	±18
ω (°)	23	±11
t_p (JD)	2456990.51	±0.03
(α_p, δ_p) (°)	(37, −40)	(±18, ±24)
(λ_p, β_p) (°)	(17, −50)	(±28, ±20)

Notes. Orbital period P, semi-major axis a, eccentricity e, inclination i, longitude of the ascending node Ω, argument of pericentre ω, time of pericentre t_p, ecliptic J2000 coordinates of the orbital pole (λ_p, β_p), and equatorial J2000 coordinates of the orbital pole (α_p, δ_p). The number of observations and RMS between the predicted and observed positions are also provided. Uncertainties are given at 1-σ.

6. Discussion and conclusion

In this Letter, we presented the discovery of S3, a third moon orbiting Elektra. The newly detected satellite revolves inside the orbit of S2 with a semi-major axis of 344 ± 5 km and an orbital period of 0.679 ± 0.001 days around the primary. Nonetheless, a lot of uncertainties remain concerning the orbit of S3. More data on S2 and S3, as well as a more thorough dynamical study are necessary to solve the problem of the motion of the satellites of Elektra. However, the discovery of the first quadruple asteroid system slightly opens the way for understanding the mechanisms of the formation of these satellites.

In terms of data processing, S3 is barely visible in the data reduced with the standard pipeline and processed with standard halo removal algorithms and it was missed until now. This shows that the development of dedicated inverse problem algorithms based on a forward modelling of the instrument is key to expanding the instrument capacities. The PIC reduction pipeline permits the suppression of artefacts that could hide small moons or lead to false detections. In addition, modelling the instrument PSF allows one to remove the asteroid halo carefully so as to increase the contrast in its surrounding. The method presented in this Letter paves the way for more robust and general approaches to reconstruct more complex PSFs of extended objects corrupted by AO corrections to study their close vicinity.

Acknowledgements. The authors would like to warmly thank the Referee Bill Merline for his pertinent feedback and remarks that helped them improving the quality and clarity of this Letter. The authors are thankful to Ferréol Soulez for the fruitful discussions. The authors thank Jules Dallant for his Keplerian orbit visualisation software which initially helped the authors to confirm that the positions fitted on S3 were consistent with a Keplerian motion. The authors also thank Anthony Boccaletti for his IDL tool we used to accurately estimate the acquisition timestamps by taking into account the overheads during the data recording. This work has made use of the SPHERE Data Centre, jointly operated by OSUG/IPAG (Grenoble), PYTHEAS/LAM/CeSAM (Marseille), OCA/Lagrange (Nice), Observatoire de Paris/LESIA (Paris), and Observatoire de Lyon/CRAL, and supported by a grant from Labex OSUG@2020, within the program 'Investissements d'Avenir' (ANR-10-LABX-56). This work was supported by the Programme National de Planétologie (PNP) of CNRS/INSU, co-funded by CNES. This work was carried out within the LabEx LIO (ANR-10-LABX-0066) of the University of Lyon, created within the framework of the Future Investments Program bearing the reference ANR-10-LABX-0066 implemented placed by the State and managed by the National Research Agency (ANR). All the reductions are based on public data provided by the ESO Science Archive Facility and acquired for different programs: 60.A-9362(A) (Yang et al., 'Origin of Multiple Asteroid Systems by Component-Resolved Spectroscopy' – 9, 30 and 31 Dec. 2014), 296.C-5038(A) (Yang et al., 'SPHERE Follow-up of the New Triple Asteroid (130) Elektra' – 16 Feb. 2016) and 199.C-0074(E) (Vernazza et al., 'Asteroids as tracers of solar system formation: Probing the interior of primordial main belt asteroids' – 30 Jul. 2019 and 6 Aug. 2019). For the initial fit of S1's orbital parameters, additional archival data are used, as detailed in Appendix C.1. The authors acknowledge the supports from Chulalongkorn University's CUniverse (CUAASC) grant and from the Program Management Unit for Human Resources & Institutional Development, Research and Innovation, NXPO (grant number B16F630069).

References

Berdeu, A., Soulez, F., Denis, L., Langlois, M., & Thiébaut, E. 2020, A&A, 635, A90
Berthier, J., Vachier, F., Marchis, F., Ďurech, J., & Carry, B. 2014, Icarus, 239, 118
Beuzit, J.-L., Vigan, A., Mouillet, D., et al. 2019, A&A, 631, A155
Carry, B., Vachier, F., Berthier, J., et al. 2019, A&A, 623, A132
Carry, B., Vernazza, P., Vachier, F., et al. 2021, A&A, 650, A129
Charbonnier, P., Blanc-Feraud, L., Aubert, G., & Barlaud, M. 1997, Trans. Image Process., 6, 298
Claudi, R. U., Turatto, M., Gratton, R. G., et al. 2008, in Ground-based and Airborne Instrumentation for Astronomy II, Proc. SPIE, 7014, 70143E
Delorme, P., Meunier, N., Albert, D., et al. 2017, in SF2A-2017: Proceedings of the Annual meeting of the French Society of Astronomy and Astrophysics, eds. C. Reylé, P. Di Matteo, F. Herpin, et al., 347
Dohlen, K., Langlois, M., Saisse, M., et al. 2008, in Ground-based and Airborne Instrumentation for Astronomy II, eds. I. S. McLean, M. M. Casali, et al., Int. Soc. Opt. Photon. (SPIE), 7014, 1266
Durech, J., Sidorin, V., & Kaasalainen, M. 2010, A&A, 513, A46
Fétick, R. J. L., Fusco, T., Neichel, B., et al. 2019, A&A, 628, A99
Fusco, T., Sauvage, J. F., Mouillet, D., et al. 2016, in Adaptive Optics Systems V, eds. E. Marchetti, L. M. Close, J. P. Véran, et al., SPIE Conf. Ser., 9909, 99090U
Gonzalez, R., Richard, E., & Steven, L. 2020, Digital Image Processing Using MATLAB, 3rd edn. (Knoxville: Gatesmark Publishing)
Hanus, J., Marchis, F., Viikinkoski, M., Yang, B., & Kaasalainen, M. 2017, A&A, 599, A36
Jovanovic, N., Martinache, F., Guyon, O., et al. 2015, PASP, 127, 890
King, O. R., Fletcher, L. N., & Ligier, N. 2019, in EPSC-DPS2019-596-1, 13
Lagarias, J. C., Reeds, J. A., Wright, M. H., & Wright, P. E. 1998, SIAM J. Optim., 9, 112
Lam, E. Y., & Goodman, J. W. 2000, J. Opt. Soc. Am. A, 17, 1177
Langlois, M., Gratton, R., Lagrange, A. M., et al. 2021, A&A, 651, A71
Maire, A.-L., Langlois, M., Delorme, P., et al. 2021, J. Astron. Telesc. Instrum. Syst., 7, 035004
Marchis, F., & Vega, D. 2014, in AGU Fall Meeting Abstracts, 2014, P43F-08
Marchis, F., Descamps, P., Hestroffer, D., & Berthier, J. 2005, Nature, 436, 822
Marchis, F., Descamps, P., Berthier, J., et al. 2008, Icarus, 195, 295
Marchis, F., Jorda, L., Vernazza, P., et al. 2021, A&A, 653, A57
Marsset, M., Carry, B., Yang, B., et al. 2016, IAU Circ., 9282, 1
Merline, W. J., Close, L. M., Dumas, C., et al. 1999, Nature, 401, 565
Merline, W. J., Weidenschilling, S. J., Durda, D. D., et al. 2002, Asteroids Do Have Satellites (Tucson, USA: University of Arizona Press), 289
Merline, W. J., Tamblyn, P. M., Dumas, C., et al. 2003, IAU Circ., 8183, 1
Miles, R., Pratt, A., & Haymes, T. 2018, J. Br. Astron. Assoc., 128, 132
Mugnier, L. M., Fusco, T., & Conan, J.-M. 2004, J. Opt. Soc. Am. A, 21, 1841
Nocedal, J. 1980, Math. Comput., 35, 773
Pajuelo, M., Carry, B., Vachier, F., et al. 2018, Icarus, 309, 134
Reddy, V., Gaffey, M. J., Abell, P. A., & Hardersen, P. S. 2012, Icarus, 219, 382
Rudin, L. I., Osher, S., & Fatemi, E. 1992, J. Phys. D, 60, 259
Schmid, H. M., Bazzon, A., Roelfsema, R., et al. 2018, A&A, 619, A9
Souami, D., Renner, S., Sicardy, B., et al. 2022, A&A, 657, A134
Soubies, E., Soulez, F., McCann, M. T., et al. 2019, Inverse Probl., 35, 104006
Soulez, F., Denis, L., Tourneur, Y., & Thiébaut, E. 2012, in 2012 9th IEEE International Symposium on Biomedical Imaging (ISBI), 1735
Thiébaut, E. 2002, Proc. SPIE, 4847, 174
Vachier, F., Berthier, J., & Marchis, F. 2012, A&A, 543, A68
Vernazza, P., Ferrais, M., Jorda, L., et al. 2021, A&A, 654, A56
Vigan, A., Fontanive, C., Meyer, M., et al. 2021, A&A, 651, A72
Wahhaj, Z., Liu, M. C., Biller, B. A., et al. 2013, ApJ, 779, 80
Yang, B., Wahhaj, Z., Beauvalet, L., et al. 2016, ApJ, 820, L35

Appendix A: Image processing: Halo removal algorithm

In Section 3, we briefly presented the image processing we developed to remove the halo of Elektra. It was applied to each acquisition, that is to say on each 2D + λ hypercube $\boldsymbol{c}^{\rm red}$ provided by the IFS reduction pipeline. The main steps, also summed up in the pseudp-code of Algorithm 1, are as follows: $\boldsymbol{d}^{\rm red}$, the reduced image, was obtained by averaging the IFS 2D + λ hypercube $\boldsymbol{c}^{\rm red}$ along its spectral dimension and was normalised to 1 (see Fig. 1(a)); $\boldsymbol{p}^{\rm core}$, the core part of the PSF, was estimated by fitting a 2D Gaussian function on the brightest moon (see Appendix A.1); $\boldsymbol{o}^{\rm dec}$, the sharp image of the primary, was obtained by deconvolving $\boldsymbol{d}^{\rm red}$ with $\boldsymbol{p}^{\rm core}$ (see Fig. 1(b) and Appendix A.2); $\boldsymbol{o}^{\rm thr}$, the primary image, was segmented by keeping only the pixels above $o^{\rm thr} > 25\%$ (see Appendix A.3); $\boldsymbol{p}^{\rm wing}$, the faint PSF extentions, were estimated by deconvolving of the halo by $\boldsymbol{o}^{\rm thr}$ (see Appendix A.3); $\boldsymbol{d}^{\rm hal}$, the model halo, is the convolution of the primary image $\boldsymbol{o}^{\rm thr}$ with the total PSF $\boldsymbol{p} = \boldsymbol{p}^{\rm core} + \boldsymbol{p}^{\rm wing}$ (see Fig. 1(d)); $\boldsymbol{d}^{\rm res}$ are the residuals after the halo model removal in which the moons are visible (see Fig. 1(e)); $\boldsymbol{d}^{\rm filt}$ was obtained by cleaning the residual background structures with a median filter (see Fig. 1(f) and Appendix A.4).

Algorithm 1 Overview of the image processing steps performed on each reduced hypercube $\boldsymbol{c}^{\rm red}$.

1: $\boldsymbol{d}^{\rm red} \underset{\text{Fig. 1(a)}}{\leftarrow} \langle \boldsymbol{c}^{\rm red}(\boldsymbol{\theta}, \lambda) \rangle_\lambda$ ▷ Spectral projection of the reduced cube
2: $\boldsymbol{p}^{\rm core} \underset{\text{Fig. A.1(b)}}{\leftarrow} \boldsymbol{d}^{\rm moon} \simeq \boldsymbol{p}^{\rm core}$ ▷ Fitting the PSF core on the brightest moon
3: $\boldsymbol{o}^{\rm dec} \underset{\text{Fig. 1(b)}}{\leftarrow} \boldsymbol{d}^{\rm red} \simeq \boldsymbol{p}^{\rm core} \star \boldsymbol{o}^{\rm dec}$ ▷ Deconvolution by the PSF core
4: $\boldsymbol{o}^{\rm thr}(\boldsymbol{\theta}) \underset{\text{Fig. A.2(a)}}{\leftarrow} \begin{cases} 0 \text{ if } \boldsymbol{o}^{\rm dec}(\boldsymbol{\theta}) \leq o^{\rm thr} \\ \boldsymbol{o}^{\rm dec}(\boldsymbol{\theta}) \text{ otherwise} \end{cases}$ ▷ Threshold on the primary
5: $\boldsymbol{p}^{\rm wing} \underset{\text{Fig. A.2(b)}}{\leftarrow} \boldsymbol{d}^{\rm red} \simeq (\boldsymbol{p}^{\rm core} + \boldsymbol{p}^{\rm wing}) \star \boldsymbol{o}^{\rm thr}$ ▷ Fitting the PSF wings
6: $\boldsymbol{d}^{\rm hal} \underset{\text{Fig. 1(d)}}{\leftarrow} (\boldsymbol{p}^{\rm core} + \boldsymbol{p}^{\rm wing}) \star \boldsymbol{o}^{\rm thr}$ ▷ Model of the halo
7: $\boldsymbol{d}^{\rm res} \underset{\text{Fig. 1(e)}}{\leftarrow} \boldsymbol{d}^{\rm red} - \boldsymbol{d}^{\rm hal}$ ▷ Residuals after removing the halo model
8: $\boldsymbol{d}^{\rm filt} \underset{\text{Fig. 1(f)}}{\leftarrow} \boldsymbol{d}^{\rm res} - f^{\rm med}(\boldsymbol{d}^{\rm res})$ ▷ Residuals of the median annulus filtering

In the following, we describe this algorithm in further detail. The code is implemented in Matlab™. The linear inverse problems use the open-source GlobalBioIm framework (Soubies et al. 2019).

A.1. Fitting the PSF core on the brightest moon

The image of the asteroid can only be obtained with the deconvolution of $\boldsymbol{d}^{\rm red}$ by the PSF. To get the details of the asteroid surface and its edges, only the core of the PSF $\boldsymbol{p}^{\rm core}$ is needed. The PSF extensions only influence large-scale structures in the data, such as the halo and thus the photometry, which are not relevant for this step. An estimate of this central part of the PSF was obtained on the brightest moon, shown in Fig. A.1(a), by fitting a 2D Gaussian function

$$\boldsymbol{p}^{\rm core}(\boldsymbol{\theta}) = g(\boldsymbol{\theta}, a, \alpha, \boldsymbol{\sigma}) \triangleq a \mathrm{e}^{-0.5(r_1^2/\sigma_1^2 + r_2^2/\sigma_2^2)}\,, \tag{A.1}$$

where $\boldsymbol{\theta} = (x, y)$ are the 2D spatial coordinates; a is the amplitude of the 2D Gaussian pattern; α is the orientation of the 2D Gaussian pattern; $r_1 = x\cos\alpha + y\sin\alpha$ and $r_2 = -x\sin\alpha + y\cos\alpha$ are the coordinates in the rotated frame of the Gaussian pattern; and $\boldsymbol{\sigma} = (\sigma_1, \sigma_2)$ are the standard deviations of the Gaussian pattern along its two axes.

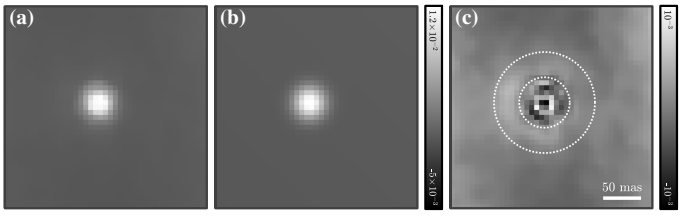

Fig. A.1. Fitting the core of the PSF on the brightest moon from Fig. A.1(c). (a) Normalised reduced data $\boldsymbol{d}^{\rm moon}$. (b) Fitted PSF model and background $\boldsymbol{p}^{\rm core} + \boldsymbol{d}^{\rm bg}$. (c) Residuals of the model. For comparison with the PSF size, the edges of the annulus filter are highlighted by the dotted white lines.

These parameters must be fitted from the data $\boldsymbol{d}^{\rm moon}$ (see Fig. A.1(a)), where an offset background $\boldsymbol{d}^{\rm bg}$ can corrupt their estimation. The background is described as follows:

$$\boldsymbol{d}^{\rm bg}(\boldsymbol{\theta}, \boldsymbol{c}) = c_0 + c_1 x + c_2 y\,, \tag{A.2}$$

where $\boldsymbol{c} = (c_0, c_1, c_2)$ is the list of the three coefficients of a one degree polynomial. In doing so, the data can be written as follows:

$$\boldsymbol{d}^{\rm moon}(\boldsymbol{\theta}) \simeq g(\boldsymbol{\theta}, a, \alpha, \boldsymbol{\sigma}) + \boldsymbol{d}^{\rm bg}(\boldsymbol{\theta}, \boldsymbol{c})\,, \tag{A.3}$$

where $\simeq$ is to symbolise the uncertainties from the noise.

All of these parameters were estimated in an alternate algorithm. First, the 2D Gaussian parameters were obtained by minimising

$$\underset{\boldsymbol{\theta}_0, a, \alpha, \boldsymbol{\sigma}}{\operatorname{argmin}} \sum_{\boldsymbol{\theta}} (\boldsymbol{d}^{\rm moon}(\boldsymbol{\theta}) - g(\boldsymbol{\theta} - \boldsymbol{\theta}_0, a, \alpha, \boldsymbol{\sigma}) - \boldsymbol{d}^{\rm bg}(\boldsymbol{\theta}, \boldsymbol{c}))^2\,, \tag{A.4}$$

by keeping $\boldsymbol{c}$ fixed and where $\boldsymbol{\theta}_0$ is the position of the moon. Then, the background parameters were estimated by solving

$$\underset{\boldsymbol{c}}{\operatorname{argmin}} \sum_{\boldsymbol{\theta}} |\boldsymbol{d}^{\rm moon}(\boldsymbol{\theta}) - g(\boldsymbol{\theta} - \boldsymbol{\theta}_0, a, \alpha, \boldsymbol{\sigma}) - \boldsymbol{d}^{\rm bg}(\boldsymbol{\theta}, \boldsymbol{c})|\,, \tag{A.5}$$

by keeping $(\boldsymbol{\theta}_0, a, \alpha, \boldsymbol{\sigma})$ fixed. Summing the absolute value is a robust method to reduce the impact of outlier pixels in the cost function.

This algorithm is summarised in Algorithm 2. The optimisation problem Eq. (A.4) is solved with the VMLM-B algorithm (Variable Metric with Limited Memory-Bounded, Thiébaut 2002), a limited-memory quasi-Newton method with BFGS updates (Broyden-Fletcher-Goldfarb-Shanno, Nocedal 1980) that handles bound constraints. The optimisation problem Eq. (A.4) is solved with the simplex search method of Lagarias et al. (1998).

Algorithm 2 Pseudo-code of the PSF core fitting on the brightest moon.

1: $\boldsymbol{c} \leftarrow \boldsymbol{0}$ ▷ Initialisation with no background
2: **for** i from 1 to 5 **do** ▷ *Five* iterations of the alternate optimisation
3: $(a, \alpha, \boldsymbol{\sigma}) \leftarrow$ solving Eq. (A.4) ▷ PSF core fitting
4: $\boldsymbol{c} \leftarrow$ solving Eq. (A.5) ▷ Background fitting

As seen in Figs. A.1(b,c), this model is sufficient to describe the core of the PSF. Figure A.1(c) also shows that the wings of the PSF cannot be fitted on the brightest moon because the signal far from its core is too noisy.

A.2. Image deconvolution

The image $\boldsymbol{o}^{\rm dec}$ of the primary was obtained by deconvolving the reduced data

$$\boldsymbol{d}^{\rm red} \simeq \boldsymbol{p}^{\rm core} \star \boldsymbol{o}^{\rm dec}, \tag{A.6}$$

where $\simeq$ is to symbolise the uncertainties from the noise. This was done by solving the minimisation problem

$$\underset{\boldsymbol{o}^{\rm dec}\geq 0}{\rm argmin}\ \mathscr{D}(\boldsymbol{d}^{\rm red}, \boldsymbol{p}^{\rm core} \star \boldsymbol{o}^{\rm dec}, \boldsymbol{w}^{\rm fov}) + \mu \mathscr{R}_{\rm 2D}(\boldsymbol{o}^{\rm dec}), \tag{A.7}$$

where $\boldsymbol{o}^{\rm dec} \geq 0$ is a positivity constraint on the reconstruction; $\boldsymbol{w}^{\rm fov}$ is the binary mask on the usable pixels of the reduced data $\boldsymbol{d}^{\rm red}$ (1 if inside the IFS field of view, see pixels colored in blue, red, and green in Fig. A.2(a)), and 0 otherwise; $\mathscr{D}(\boldsymbol{d}^{\rm red}, \boldsymbol{p}^{\rm core} \star \boldsymbol{o}^{\rm dec}, \boldsymbol{w}^{\rm fov})$ is the data fidelity term between the $\boldsymbol{d}^{\rm red}$ and the model $\boldsymbol{p}^{\rm core} \star \boldsymbol{o}^{\rm dec}$ weighted by $\boldsymbol{w}^{\rm fov}$

$$\mathscr{D}(\boldsymbol{\varphi}_1, \boldsymbol{\varphi}_2, \boldsymbol{w}) \triangleq \sum_{\boldsymbol{\theta}\ \text{s.t.}\ \boldsymbol{w}(\boldsymbol{\theta})=1} (\boldsymbol{\varphi}_1(\boldsymbol{\theta}) - \boldsymbol{\varphi}(\boldsymbol{\theta})_2)^2\,; \tag{A.8}$$

$\mathscr{R}_{\rm 2D}(\boldsymbol{o}^{\rm dec})$ is a regularisation term that favours sharp-edged objects to control the spatial continuity and smoothness of the reconstruction; and μ is the hyperparameter to weigh the regularisation compared to the data fidelity term.

Enforcing an edge-preserving smoothness via $\mathscr{R}_{\rm 2D}(\boldsymbol{o}^{\rm dec})$ was done by encouraging the sparsity of spatial gradients (Rudin et al. 1992; Charbonnier et al. 1997):

$$\mathscr{R}_{\rm 2D}(\boldsymbol{\varphi}) \triangleq \sum_{\boldsymbol{\theta}} [\sqrt{([\boldsymbol{\nabla}_x \boldsymbol{\varphi}(\boldsymbol{\theta})]^2 + [\boldsymbol{\nabla}_y \boldsymbol{\varphi}(\boldsymbol{\theta})]^2 + \epsilon^2)} - \epsilon], \tag{A.9}$$

where $\boldsymbol{\nabla}_x$ and $\boldsymbol{\nabla}_y$ correspond to finite difference operators along the first and second spatial dimensions, respectively, and $\epsilon > 0$ is a threshold corresponding to the smallest gradient at a sharp edge and it ensures that this hyperbolic approximation of the Euclidean norm is differentiable at zero.

The optimisation problem Eq. (A.7) was solved by the VMLM-B algorithm (Thiébaut 2002). The value of $\epsilon = 3 \times 10^{-2}$ and $\mu = 5 \times 10^{-3}$ were manually tuned to give a sharp image while limiting the flat areas.

As seen in Fig. 1(b), this deconvolution successfully provides an image $\boldsymbol{o}^{\rm dec}$ of Elektrawith sharp edges with some spatial features on its surface. As the PSF extensions have not been included in the model yet, this reconstruction is still corrupted by the asteroid halo. Thus, this image is segmented to extract the primary $\boldsymbol{o}^{\rm thr}$ from its halo by keeping only the pixels above $o^{\rm thr} > 25\%$, emphasised by the green pixels in Fig. A.2(a).

A.3. Halo fitting

Once the detailed image of the asteroid $\boldsymbol{o}^{\rm thr}$ was reconstructed, the PSF extensions $\boldsymbol{p}^{\rm wing}$ could be estimated. This is similar to deconvolving the data by the primary image to obtain the PSF wings. The model of $\boldsymbol{p}^{\rm wing}$ was fitted only on the halo. As a consequence, the pixels of the primary of $\boldsymbol{o}^{\rm thr}$ were rejected (as seen in green in Fig. A.2(a)). In addition, to avoid any impact of the core of the PSF $\boldsymbol{p}^{\rm core}$ close to the edges of the asteroid, this mask was further morphologically eroded by 5 pixels (Gonzalez et al. 2020) (in red in Fig. A.2(a)). This roughly corresponds to the radius of the PSF (see Fig. A.1). And, as previously done, the pixels outside the IFS field of view were also rejected. In total, only the pixels $\boldsymbol{w}^{\rm hal}$ (in blue in Fig. A.2(a)) were kept to fit the halo from the data $\boldsymbol{d}^{\rm red}$.

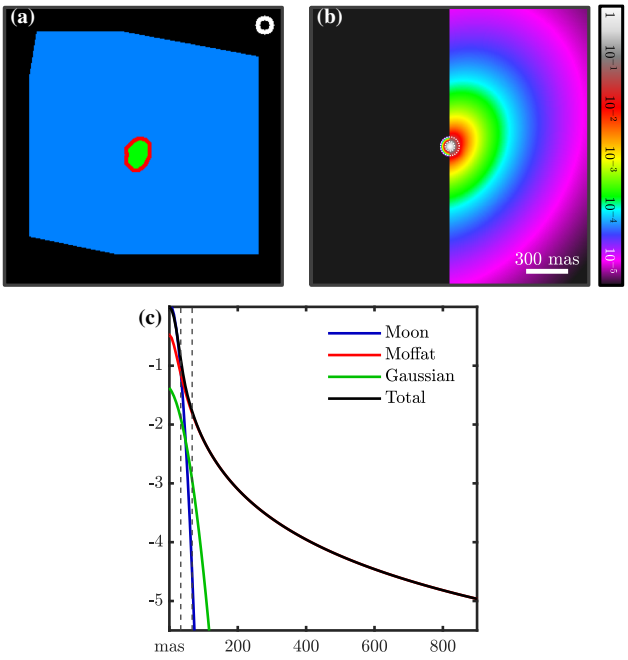

Fig. A.2. Fitting the PSF wings from Figs. 1(b,c) and Fig. A.1(b). (a) Map of the different mask on the pixel. Green: pixels of the primary after segmentation. Red: pixels removed after the primary mask erosion. Black: pixels outside the IFS field of view. Blue: pixels on which the halo was fitted and the median filter applied. It should be noted that the annulus filter is displayed in white. (b) Comparison of the core of the PSF $\boldsymbol{p}^{\rm core}$ of Fig. A.1(b) (left) with the total PSF $\boldsymbol{p}^{\rm core} + \boldsymbol{p}^{\rm wing}$ fitted by accounting for the halo (right) (logarithmic scale). The dotted white lines emphasise the edges of the annulus median filter. (c) x-profiles of (b) (logarithmic scale). The different components of the PSF are emphasised by different colours. Blue: PSF core $\boldsymbol{p}^{\rm core}$ fitted on the brightest moon (normalised to its maximal value). Black: total PSF $\boldsymbol{p}^{\rm core} + \boldsymbol{p}^{\rm wing}$ (normalised to its maximal value). Red: Moffat sub-part m of the PSF wings $\boldsymbol{p}^{\rm wing}$ (normalised to the total PSF maximal value). Green: Gaussian sub-part g of the PSF wings $\boldsymbol{p}^{\rm wing}$ (normalised to the total PSF maximal value). Dashed grey lines: edges of the annulus median filter.

The model of the PSF wings is a summation of a 2D Gaussian function and a 2D Moffat function

$$\boldsymbol{p}^{\rm wing}(\boldsymbol{\theta}) = g(\boldsymbol{\theta} - \boldsymbol{\theta}_0, a, \alpha, \boldsymbol{\sigma}) + m(\boldsymbol{\theta} - \tilde{\boldsymbol{\theta}}_0, \tilde{a}, \tilde{\alpha}, \tilde{\beta}, \tilde{\boldsymbol{\sigma}}) \tag{A.10}$$

$$\triangleq a e^{-0.5(r_1^2/\sigma_1^2 + r_2^2/\sigma_2^2)} + \tilde{a}(1 + \tilde{r}_1^2/\sigma_1^2 + \tilde{r}_2^2/\sigma_2^2)^{-\tilde{\beta}}, \tag{A.11}$$

where the 2D Gaussian function g and its parameters $(a, \alpha, \boldsymbol{\sigma})$ are defined as in Eq. (A.1); $\tilde{a}$ is the amplitude of the 2D Moffat pattern; $\tilde{\alpha}$ is the orientation of the 2D Moffat pattern; $\tilde{\beta}$ is the power parameter of the 2D Moffat pattern; $\tilde{r}_1 = (x - \tilde{x}_0)\cos\tilde{\alpha} + (y - \tilde{y}_0)\sin\tilde{\alpha}$ and $\tilde{r}_2 = -(x - \tilde{x}_0)\sin\tilde{\alpha} + (y - \tilde{y}_0)\cos\tilde{\alpha}$ are the coordinates in the rotated frame of the Moffat pattern; and $\tilde{\boldsymbol{\sigma}} = (\tilde{\sigma}_1, \tilde{\sigma}_2)$ are the extensions of the Moffat pattern along its two axes. The positions $\boldsymbol{\theta}_0$ and $\tilde{\boldsymbol{\theta}}_0$ were let free to account for a possible non-symmetry in the PSF wing, which is shifted compared to the PSF core.

As for the PSF core, a background can corrupt the PSF wings' estimate and it was consequently fitted within the halo model $\boldsymbol{d}^{\rm hal}$

$$\boldsymbol{d}^{\rm red}(\boldsymbol{\theta}) \simeq \boldsymbol{p}^{\rm core}(\boldsymbol{\theta}) \star \boldsymbol{o}^{\rm thr}(\boldsymbol{\theta}) \tag{A.12}$$

$$+ g(\boldsymbol{\theta} - \boldsymbol{\theta}_0, a, \alpha, \boldsymbol{\sigma}) \star \boldsymbol{o}^{\rm thr}(\boldsymbol{\theta}) \tag{A.13}$$

$$+ m(\boldsymbol{\theta} - \tilde{\boldsymbol{\theta}}_0, \tilde{a}, \tilde{\alpha}, \tilde{\beta}, \tilde{\boldsymbol{\sigma}}) \star \boldsymbol{o}^{\rm thr}(\boldsymbol{\theta}) \tag{A.14}$$

$$+ \boldsymbol{d}^{\mathrm{bg}}(\boldsymbol{\theta}, \boldsymbol{c}) \tag{A.15}$$

$$\triangleq \boldsymbol{d}^{\mathrm{hal}}(\boldsymbol{\theta}, \boldsymbol{\theta}_0, a, \alpha, \boldsymbol{\sigma}, \tilde{\boldsymbol{\theta}}_0, \tilde{a}, \tilde{\alpha}, \tilde{\beta}, \tilde{\boldsymbol{\sigma}}, \boldsymbol{c}) \,, \tag{A.16}$$

where $\simeq$ is to symbolise the uncertainties from the noise for $\boldsymbol{w}^{\mathrm{hal}}(\boldsymbol{\theta}) = 1$.

Similar to the PSF core fitting in Section A.1, all these parameters were estimated in an alternate algorithm. First, the 2D Moffat parameters were obtained by minimising

$$\underset{\tilde{\boldsymbol{\theta}}_0, \tilde{a}, \tilde{\alpha}, \tilde{\beta}, \tilde{\boldsymbol{\sigma}}}{\operatorname{argmin}} \sum_{\boldsymbol{\theta} \text{ s.t. } \boldsymbol{w}^{\mathrm{hal}}(\boldsymbol{\theta})=1} \Big(\boldsymbol{d}^{\mathrm{red}}(\boldsymbol{\theta}) - \boldsymbol{d}^{\mathrm{hal}}(\boldsymbol{\theta}, \boldsymbol{\theta}_0, a, \alpha, \boldsymbol{\sigma}, \tilde{\boldsymbol{\theta}}_0, \tilde{a}, \tilde{\alpha}, \tilde{\beta}, \tilde{\boldsymbol{\sigma}}, \boldsymbol{c}) \Big)^2 \tag{A.17}$$

by keeping $(\boldsymbol{\theta}_0, a, \alpha, \boldsymbol{\sigma}, \boldsymbol{c})$ fixed. Then, the 2D Gaussian parameters were obtained by minimising

$$\underset{\boldsymbol{\theta}_0, a, \alpha, \boldsymbol{\sigma}}{\operatorname{argmin}} \sum_{\boldsymbol{\theta} \text{ s.t. } \boldsymbol{w}^{\mathrm{hal}}(\boldsymbol{\theta})=1} \Big(\boldsymbol{d}^{\mathrm{red}}(\boldsymbol{\theta}) - \boldsymbol{d}^{\mathrm{hal}}(\boldsymbol{\theta}, \boldsymbol{\theta}_0, a, \alpha, \boldsymbol{\sigma}, \tilde{\boldsymbol{\theta}}_0, \tilde{a}, \tilde{\alpha}, \tilde{\beta}, \tilde{\boldsymbol{\sigma}}, \boldsymbol{c}) \Big)^2 \tag{A.18}$$

by keeping $(\tilde{\boldsymbol{\theta}}_0, \tilde{a}, \tilde{\alpha}, \tilde{\beta}, \tilde{\boldsymbol{\sigma}}, \boldsymbol{c})$ fixed. Finally, the background parameters were estimated by solving

$$\underset{\boldsymbol{c}}{\operatorname{argmin}} \sum_{\boldsymbol{\theta} \text{ s.t. } \boldsymbol{w}^{\mathrm{hal}}(\boldsymbol{\theta})=1} \Big| \boldsymbol{d}^{\mathrm{red}}(\boldsymbol{\theta}) - \boldsymbol{d}^{\mathrm{hal}}(\boldsymbol{\theta}, \boldsymbol{\theta}_0, a, \alpha, \boldsymbol{\sigma}, \tilde{\boldsymbol{\theta}}_0, \tilde{a}, \tilde{\alpha}, \tilde{\beta}, \tilde{\boldsymbol{\sigma}}, \boldsymbol{c}) \Big| \,, \tag{A.19}$$

by keeping $(\boldsymbol{\theta}_0, a, \alpha, \boldsymbol{\sigma}, \tilde{\boldsymbol{\theta}}_0, \tilde{a}, \tilde{\alpha}, \tilde{\beta}, \tilde{\boldsymbol{\sigma}})$ fixed.

This algorithm is summarised in Algorithm 3. The optimisation problems seen in Eqs. (A.17,A.18) were solved by the VMLM-B algorithm (Thiébaut 2002). The optimisation problem in Eq. (A.19) was solved by the simplex search method of Lagarias et al. (1998).

Algorithm 3 Pseudo-code of the PSF wings' fitting on the halo of the primary.

$\boldsymbol{c} \leftarrow \boldsymbol{0}$ ▷ Initialisation with no background
$a \leftarrow 0$ ▷ Initialisation with no Gaussian pattern
for i from 1 to 10 **do** ▷ *Ten* iterations of the alternate optimisation
  $(\tilde{\boldsymbol{\theta}}_0, \tilde{a}, \tilde{\alpha}, \tilde{\beta}, \tilde{\boldsymbol{\sigma}}) \leftarrow$ solving Eq. (A.17) ▷ 2D Moffat pattern fitting
  $(\boldsymbol{\theta}_0, a, \alpha, \boldsymbol{\sigma}) \leftarrow$ solving Eq. (A.18) ▷ 2D Gaussian pattern fitting
  $\boldsymbol{c} \leftarrow$ solving Eq. (A.19) ▷ Background fitting

The results are presented in Figs. A.2(b,c). It first appears from Fig. A.2(b) that the PSF wings are elongated and not radially symmetric. The PSF orientation follows that of Elektra's halo in Fig. 1(c). Then, the comparison in Fig. A.2(c) of the profile of the PSF core $\boldsymbol{p}^{\mathrm{core}}$ fitted on the moon (in blue), with the profile of the final total PSF $\boldsymbol{p}^{\mathrm{core}} + \boldsymbol{p}^{\mathrm{wing}}$ in black, shows that the shape of the PSF core, below the first dashed line, is not changed by the fit of the wings. And beyond this radius, the PSF profile is dominated by its wings, mainly approximated by the Moffat profile (in red). This validates our 'core + wings' approach and its fitting strategy. Finally, these curves also show that the additional 2D Gaussian pattern (in green) only plays a minor role, slightly more extended than the PSF core, meaning that it mainly impacts the halo close to the primary.

Looking at the edges of the median filter (the grey dashed lines in Fig. A.2(c)), it appears that the PSF wing intensity is a few percent of its maximal value in the filter domain. This is consistent with the residual structures inside the median filter mask on Fig. A.1(c), beyond the PSF core. In case one wants to obtain the absolute photometry, a constant correction factor must be applied that can be fitted on the PSF model. This is nonetheless beyond the scope of this Letter and does impact our photometry study based on photometric ratios.

A.4. Median filter

Once the total PSF was estimated as described in Appendix A.3, the model of the halo $\boldsymbol{d}^{\mathrm{hal}}$ defined in Eq. (A.16) was removed from the reduced data

$$\boldsymbol{d}^{\mathrm{res}}(\boldsymbol{\theta}) = \boldsymbol{d}^{\mathrm{red}}(\boldsymbol{\theta}) - \boldsymbol{d}^{\mathrm{hal}}(\boldsymbol{\theta}, \boldsymbol{\theta}_0, a, \alpha, \boldsymbol{\sigma}, \tilde{\boldsymbol{\theta}}_0, \tilde{a}, \tilde{\alpha}, \tilde{\beta}, \tilde{\boldsymbol{\sigma}}, \boldsymbol{c}) \,. \tag{A.20}$$

These residuals are shown in Fig. 1(e). Most of the halo was successfully removed, as expected, close to the primary edges and the moons are better visible. Nonetheless some spatially extended structures remain that can be attributed to the instrument background or the sky background.

To further clean these artefacts, a median filter was applied on this residual map. To prevent any self-subtraction, the shape of this filter is an annulus whose inner (resp. outer) diameter is once (resp. twice) the PSF core size. The idea is to correct for local background features, hence the disc shape, while preventing self-subtraction of the moon due to the core of the PSF, hence the annulus. The shape of this annulus is given in Fig. A.1(c) and Figs. A.2(a,b). It must be compared with the PSF core size: its inner diameter is 5 pixels, corresponding to the size of the PSF core, and its outer diameter is twice this value, that is to say 10 pixels.

This median filter is applied only on the pixels given by $\boldsymbol{w}^{\mathrm{hal}}$, in blue in Fig. A.2(a), as described in Algorithm 4.

Algorithm 4 Pseudo-code of the median filtering with an annulus mask.

$\boldsymbol{d}^{\mathrm{filt}} \leftarrow \boldsymbol{0}$ ▷ Initialisation with zeros
$r^{\mathrm{in}} \leftarrow 5$ ▷ Annulus mask's inner radius
$r^{\mathrm{out}} \leftarrow 10$ ▷ Annulus mask's outer radius
for $\boldsymbol{\theta}$ s.t. $\boldsymbol{w}^{\mathrm{hal}}(\boldsymbol{\theta}) = 1$ **do** ▷ Filtering only the pixels in $\boldsymbol{w}^{\mathrm{hal}}$
  $\vartheta \leftarrow \mathrm{med}\left[\boldsymbol{d}^{\mathrm{res}}\left(\tilde{\boldsymbol{\theta}} \text{ s.t. } \begin{cases} \boldsymbol{w}^{\mathrm{hal}}(\tilde{\boldsymbol{\theta}}) = 1 \\ r^{\mathrm{in}} \leq \|\tilde{\boldsymbol{\theta}} - \boldsymbol{\theta}\| \leq r^{\mathrm{out}} \end{cases} \right) \right]$ ▷ Median value
  $\boldsymbol{d}^{\mathrm{filt}}(\boldsymbol{\theta}) \leftarrow \boldsymbol{d}^{\mathrm{res}}(\boldsymbol{\theta}) - \vartheta$ ▷ Removing the median filter

The result of this median filtering, $\boldsymbol{d}^{\mathrm{filt}}$, is given in Fig. 1(f). Most of the background structures are efficiently removed. The only remaining artefacts have a size similar to the PSF core. The three moons are now clearly visible in a single acquisition frame.

Appendix B: Comparison with the SPHERE/DC reduction pipeline

For comparison purposes, we present in this section the results obtained using the reduction pipeline of the SPHERE Data Centre (SPHERE/DC, Delorme et al. 2017). The same image processing steps were applied on the hypercubes to estimate and remove the halo.

The reduced projection in Fig. B.1(a) presents vertical artefacts that corrupt the image deconvolution. They are interpreted as a misalignment between the calibrations and the science images (Berdeu et al. 2020), a parameter that is estimated, and thus corrected, by the PIC reduction pipeline.

Comparing Fig. B.1(b) with Fig. 1(b), it is clear that these artefacts induce the reconstructed image of the asteroid surface

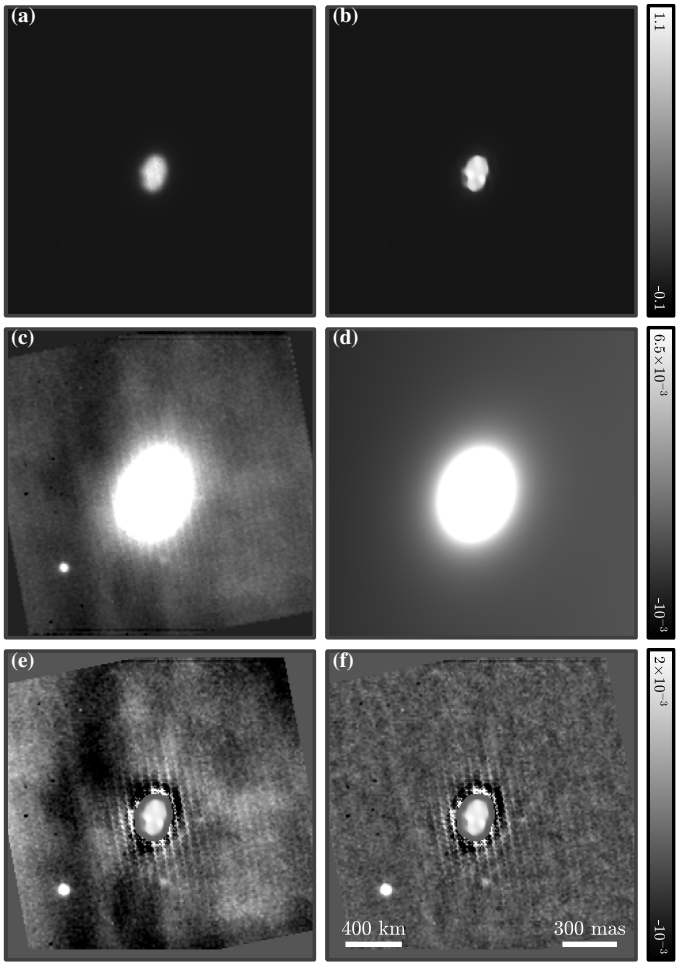

Fig. B.1. Overview of the image processing steps, applied on the 24th acquisition of 9 Dec. 2014 after its reduction by the SPHERE/DC pipeline (Delorme et al. 2017). See caption of Fig. 1.

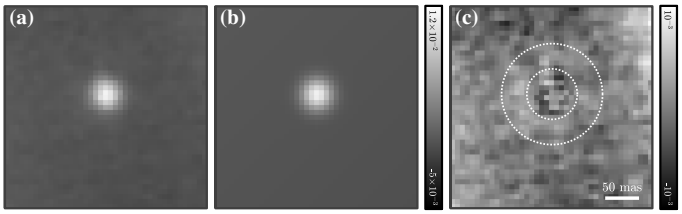

Fig. B.2. Fitting the core of the PSF on the brightest moon from Fig. B.1(c). See caption of Fig. A.1.

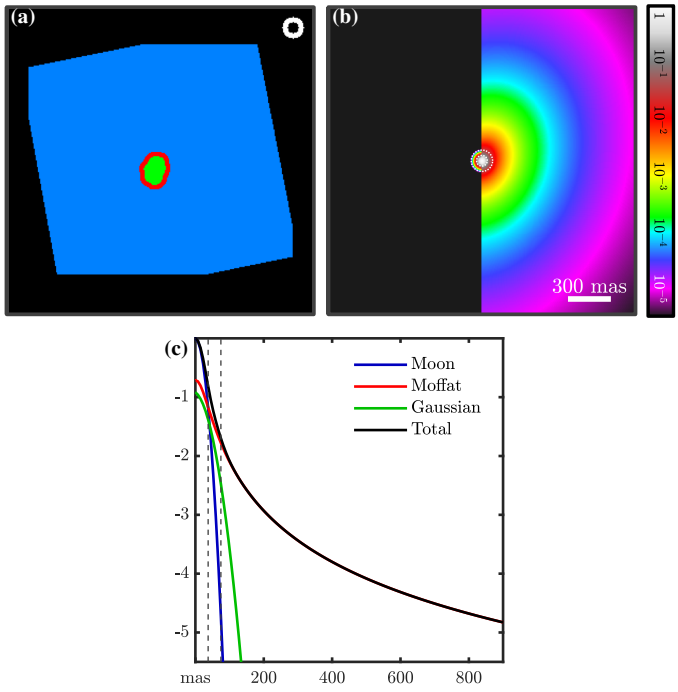

Fig. B.3. Fitting the PSF wings from Figs. B.1(b,c) and Fig. B.2(b). See caption of Fig. A.2.

to be less smooth and homogeneous than with the PIC reduction pipeline. This can impact the halo fitting accuracy. But above all, this can bias the integrated flux from the primary and its centroiding, degrading the quality of the astrophotometry fit.

These artefacts are also clearly seen in the saturated view given in Fig. B.1(c). They cannot be removed by the halo fitting (see Fig. B.1(e)), nor by the median filtering (see Fig. B.1(f)). As a consequence, the faint third moon can be mistaken with these artefacts. On the contrary, this moon is obvious in the data processed after the reduction by PIC (in Fig. 1(f)).

Comparing the time-lapses of the data reduction and processing of Visualisations 1 and 5[4] leads to the same conclusions. The PIC pipeline provides a smoother and less noisy background than the SPHERE/DC pipeline. The third moon motion is also barely visible behind the parallel artefacts.

Comparing the residuals of the PSF core fitting in Fig. A.1(c) and Fig. B.2(c), it clearly appears that the reduction with the PIC pipeline is less noisy. Some features in the PSF wing are even visible in Fig. A.1(c), while being completely erased in the noise with the SPHERE/DC reduction in Fig. B.2(c). This further confirms that adequate regularisations and priors in the IFS raw data reduction can push forward the instrument contrast and detection limits.

[4] https://www.aanda.org/10.1051/0004-6361/202142623/olm

Figure B.3 presents the fit of the PSF wings. It shows that it is consistent with the fit obtained for the data reduced with PIC in Fig. A.2. This supports the fact that our parametric method, which depends on a limited number of parameters to describe the PSF, is robust to local artefacts.

Finally, Fig. B.4 summarises the performances of the moon fitting strategy applied on the processed data after their reduction with the two pipelines. It first appears that the dispersion of the moon positions fitted on each frame (dots) is higher with the SPHERE/DC pipeline (dark red) than with PIC (dark blue). This is particularly visible on the angle (middle column): with the PIC pipeline, the temporal evolution follows a monotonous trend whereas the SPHERE/DC pipeline produces a lot more outliers. This can also be seen in the xy-position plane where the dispersion around the polar linear fit (plain curve) is reduced with PIC. Then, looking at the separation and xy-position evolution of S1(red) and S2 (green), a constant bias can be noticed between the two pipelines. These biases correspond to a shift in the linear fits of $(\delta x, \delta y) \simeq (1.8, -3.9)$ mas for S1and $(\delta x, \delta y) \simeq (1.5, -3.6)$ mas for S2. The similarity of these values allows one to argue in favour of a bias in the primary centre estimation rather than a plate scale error, which would produce a shift proportional with the distance to the primary. As mentioned earlier, the artefacts of the SPHERE/DC pipeline are present in the

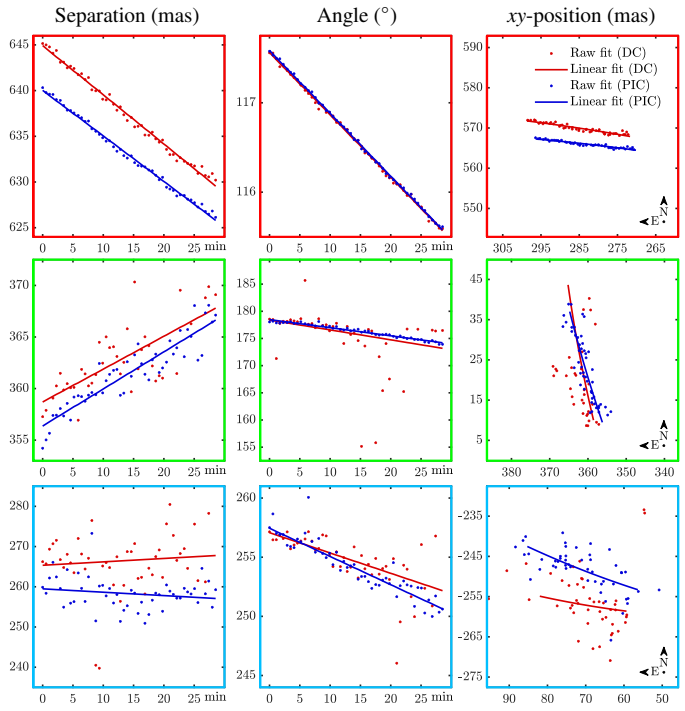

Fig. B.4. Comparison of the moon position fitting for the SPHERE/DC (dark red) and PIC pipelines (dark blue) for the three moons: S1 (first line, red frame), S2 (second line, green frame), and S3 (third line, blue frame). The positions are given in polar coordinates, separation (first column), and angle (second column) as well as Cartesian coordinates (xy-positions, third column). The dots are the position individually fitted in each acquisition. The curves are the temporal linear fits performed on the polar coordinates.

deconvolved image of Elektraand can bias the estimate of its photocentre. Finally, the offset between the two pipelines on S3 (blue), $(\delta x, \delta y) \simeq (-0.3, 8.7)$ mas, can be attributed to the stripe-shaped artefacts in the SPHERE/DC reduction that bias the estimation of the moon position. This can also be seen in Visualisation 5[5] where the motion of S3 seems to follow one from this artefact stripe.

Appendix C: Discussion on the orbital fit

In this appendix, we discuss the twofold degeneracy in the orbital pole fit and we list the orbital elements of S1 and S2 as well as the spin alignment of the different moons.

C.1. Degeneracy of the orbital pole

With datasets spanning from 9 Dec. to 31 Dec. 2014, it could be expected that the change in the viewing angle of the system, of only 3.6°, is insufficient to lift the twofold degeneracy in the orbital pole. This degeneracy originates from the projection of a 3D ellipse onto the 2D plane tangent to the observation direction.

Concerning the degeneracy on S1, we recall here that the system mass and the orbital parameters of S1were initialised on archival data spanning from 2003 to 2019, as detailed in Table C.1. In these datasets, the system was viewed from many angles and the orbital pole of S1was unequivocally determined.

[5] https://www.aanda.org/10.1051/0004-6361/202142623/olm

Table C.1. List of the archival data used for the orbital fit initialisation.

Year (n_{obs})	Instrument	PI	Programme
2003 (1)	Keck II / NIRC2	Merline B.	N22N2
2003 (1)	Keck II / NIRC2	de Pater I.	U37N2
2004 (3)	VLT / NACO	Marchis F.	072.C-0016(A)
2004 (2)	VLT / NACO	Merline B.	072.C-0753(A)
2004 (2)	Gem-N / NIRI	Merline B.	GN-2004B-C-5
2005 (2)	Keck II / NIRC2	de Pater I.	U58N2
2006 (1)	Gem-N / NIRI	Berthier J.	GN-2006A-Q-75
2006 (2)	VLT / NACO	Marchis F.	077.C-0422(A)
2008 (1)	Keck II / NIRC2	Conrad A. & Merline B. (Armandroff T.)	K208N2L
2012 (1)	VLT / NACO	Marchis F.	089.C-0944(B)
2016 (1)	VLT / NACO	Carry B.	095.C-0618(B)
2019 (6)	VLT / ZIMPOL	Vernazza P.	199.C-0074(E)

Notes. We note that n_{obs} is the number of observations used in each observation programme directed by the principal investigator (PI).

Table C.2. Orbital pole fit for the different symmetry on S2 and S3.

	$\delta_{\uparrow}(°)$	RMS (mas)	χ^2_ν
S1 / S2 / S3	6°/4°/38°	6.77	1.34
S1 / S2* / S3	5°/116°/39°	7.02	1.53
S1 / S2 / S3*	6°/2°/70°	8.48	1.98
S1 / S2* / S3*	5°/118°/77°	9.03	2.25

Notes. We note that $\delta_{\uparrow}$is the relative orientation of the moon pole orbit and Elektra's spin axis. For a given moon S, S denotes the solution presented in this Letter, and S* is for its pole orbit symmetry. Furthermore, χ^2_ν is the reduced χ^2 statistic of the fit.

This solution was thus kept to fit the orbits of S2 and S3 in the 2014 datasets.

In the main text in Section 5, we provide the orbital elements of S3 fitted by Genoid. They correspond to the best solution found by the genetic-based algorithm, looking at all the possible combinations of the different parameters. This means that one orbital pole solution was chosen by the algorithm for S2 and S3.

In the following, we forced Genoid to fit the best solution on each orbital pole for S2 and S3 to quantify their orbital pole degeneracy. We checked if the four possible symmetries are equivalent or if the one given in this Letter indeed prevails. The results are given in Table C.2. In the following, for a given moon S, S denotes the solution presented in this Letter, and S* is for its pole orbit symmetry.

It appears that the quality of the astrometry obtained after the robust linear fit helps Genoid to favour one solution out of the three. Concerning S3 (whatever the symmetry on S2), the reduced χ^2 statistic, χ^2_ν, on S3* is $\geq 45\%$ worse than the one on S3. Genoid thus strongly pulls towards the S3 symmetry, rejecting S3*. For S2 (whatever the symmetry on S3), the symmetry breaking is less obvious, the χ^2_ν being only slightly better for the S2 symmetry than for S2* by $\sim 15\%$. Similar conclusions were obtained looking at the RMS error.

Beyond the reduced χ^2_ν optimal value, other physics-based arguments support the S2/S3 symmetry. Enforcing the S2* symmetry, whatever the symmetry on S3, leads to an orientation of S2's pole orbit relative to Elektra's spin axis of about $\sim 117°$, that is to say a retrograde and polar orbit that is highly improbable. Then, whatever the symmetry on S2, the S3 symmetry

Table C.3. Orbital elements of S1and S2, expressed in EQJ2000.

S1 – S/2003 (130) 1		
Observing data set		
Number of observations	150	
Time span (days)	22	
RMS (mas)	3.53	
Orbital elements EQJ2000		
P (day)	5.287	± 0.004
a (km)	1353	± 17
e	0.09	± 0.02
i (°)	161	± 1
Ω (°)	179	± 3
ω (°)	179	± 7
t_p (JD)	2456990.85	± 0.08
(α_p, δ_p) (°)	(89, −71)	(±3, ±1)
(λ_p, β_p) (°)	(277, −87)	(±20, ±2)
S2 – S/2014 (130) 1		
Observing data set		
Number of observations	120	
Time span (days)	22	
RMS (mas)	2.39	
Orbital elements EQJ2000		
P (day)	1.192	± 0.002
a (km)	501	± 7
e	0.03	± 0.03
i (°)	156	± 7
Ω (°)	187	± 10
ω (°)	235	± 18
t_p (JD)	2456990.53	± 0.06
(α_p, δ_p) (°)	(97, −66)	(±10, ±7)
(λ_p, β_p) (°)	(165, −87)	(±113, ±4)

Notes. Orbital period P, semi-major axis a, eccentricity e, inclination i, longitude of the ascending node Ω, argument of pericentre ω, time of pericentre t_p, ecliptic J2000 coordinates of the orbital pole (λ_p, β_p), and equatorial J2000 coordinates of the orbital pole (α_p, δ_p). The number of observations and RMS between the predicted and observed positions are also provided. Uncertainties are given at 1-σ.

Table C.4. Spin alignment of all components of Elektra.

Spin alignment		
S.A. Elektra vs *P.O.* S1	6°	± 1°
S.A. Elektra vs *P.O.* S2	4°	± 5°
S.A. Elektra vs *P.O.* S3	38°	± 19°
P.O. S1 vs *P.O.* S2	5°	± 5°
P.O. S1 vs *P.O.* S3	40°	± 21°
P.O. S2 vs *P.O.* S3	42°	± 20°

Notes. Given at initial condition at Julian date: 2456990. For Elektra, we use $(\lambda, \beta) = (64°, -88°)$ as the ecliptic J2000 longitude and latitude, respectively, of the spin axis *S.A.* available on the Database of Asteroid Models from Inversion Techniques (DAMIT, Durech et al. 2010), and pole orbit *P.O.* of a satellite.Uncertainties are given at 1-σ.

solution chosen by Genoid is very inclined (∼ 38.5°) compared to Elektra's spin axis, but still twice less than its symmetry solution S3* (∼ 73.5°), which is once again an unfavourable polar orbit situation. Finally, with this S2/S3 solution, the three moons revolve in the same sense as Elektra's spin, which is a reassuring feature. This solution is the one presented in this Letter.

C.2. Orbital elements of S1and S2

The parameters of S2 were already fitted on the same 2014 datasets by Yang et al. (2016). As the fit presented in this Letter gives a lower RMS of 2.4 mas on the moon orbit model, we present this refined set of dynamical parameters for the orbital elements of S2 in Table C.3.

On the other side, the elements of S1in Table C.3 must be handled with care. Indeed, they correspond to the fit performed in this Letter, only on the 2014 datasets, despite being initialised on data spanning from 2003 to 2019 as discussed in Appendix C.1. Using these additional observations, spanning over a period of 16 years, to perform a global fit would provide more precise parameters. However, this is beyond the scope of this Letter.

C.3. Spin alignment

Table C.4 presents the spin alignment of all components of the Elektrasystem in the global fit obtained by Genoid for the symmetry presented in this Letter ($S2/S3$).

Appendix D: Hints of detections in other datasets

IRDIS/IFS and ZIMPOL are not sensitive to the same wavelength range. This makes them complementary instruments to study asteroid systems.

IRDIS/IFS – On one side, as described in this Letter, the more extended spatial structure of the halo in IFS data (the position of the AO cutoff frequency in the PSF is proportional to the wavelength) makes it easier to model close to the primary. In addition, the better AO performances in the NIR bands allow one to reach very good contrast and opens the path to detect new moons orbiting the primary vicinity, similarly to S3. Nonetheless, in this spectral range, the sky produces a non-negligible background signal, as seen in Fig. 1(e), possibly hiding the faintest targets.

ZIMPOL – On the other side, without any internal heat production, these asteroids mainly reflect the sunlight and thus are slightly brighter in the visible band of ZIMPOL than in the NIR sensitivity range of IRDIS and the IFS. In addition, the sky background is negligible in this wavelength range (Beuzit et al. 2019). One can consequently hope to detect fainter (and thus smaller) moons orbiting asteroids at smaller separation with ZIMPOL. But at these smaller wavelengths, the AO system is less efficient and could leave a higher amount of scattered light around the primary. In addition the PSF of ZIMPOL is spatially more complicated than the PSF of the IFS since the AO cutoff frequency comes closer to the primary (see e.g., Fétick et al. 2019; Marchis et al. 2021). If the contrast is thus expected to be better far from the primary than in the IFS, the halo removal close to the asteroid remains a challenge where the IFS can provide complementary performances. This complementarity can also be useful to compare moons albedo with different instruments (visible v.s.NIR) to provide insights on their surface chemical composition (Reddy et al. 2012).

Following the discovery of S2, 140 additional SPHERE/IFS observations were performed on 16 Feb 2016 by Yang et al. (296.C-5038(A) – 'SPHERE Follow-up of the New Triple Asteroid (130) Elektra'). They were reduced with the PIC pipeline and processed as described in Section 3. Their temporal median projection is given in Fig. D.1. The time-lapse

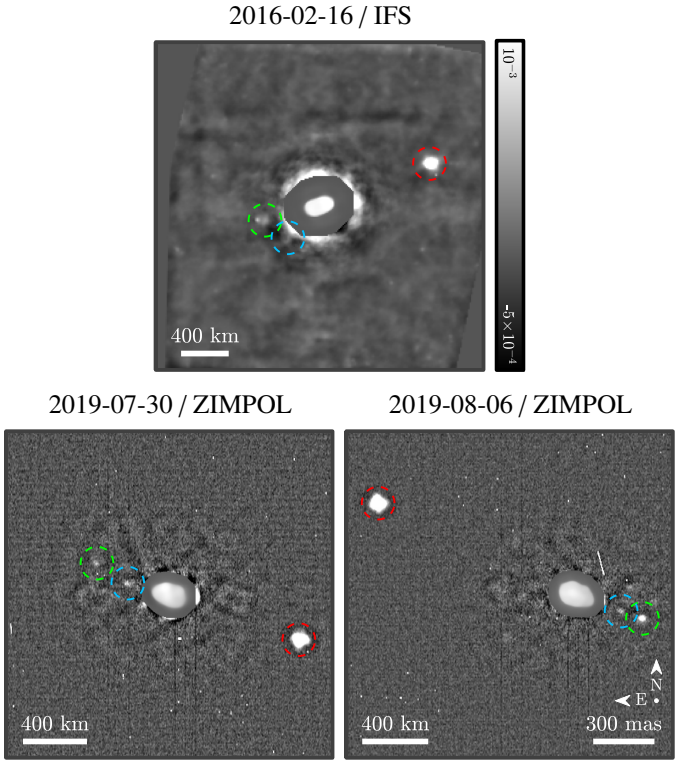

Fig. D.1. Strong hints of detection in other datasets. The dashed circles indicate manually pinned positions on what could be a moon signal in the data. The central part of the field of view has been replaced by a dimmer deconvolved image of Elektrato simultaneously visualise the primary and the moons. IFS: Median projection of 140 acquisitions. ZIMPOL: Single acquisition of each observation night.

of the data reduction and processing is given in Visualisation 4[6]. The conditions of observation were less favourable than in Dec. 2014: the seeing was worse (∼ 1.1″ versus ∼ 0.7″ for 9 Dec. 2014) and Elektrawas sss20% further along. We circle in Fig. D.1 what could be S3 without insuring that this is a detection.

Data were also gathered in Jul and Aug 2019 in the context of the systematic survey of main belt asteroids by Vernazza et al. (2021) with ZIMPOL (199.C-0074(E) – 'Asteroids as tracers of solar system formation: Probing the interior of primordial main belt asteroids'). As mentioned above, the halo removal algorithm presented in this Letter is not adapted to correctly model the halo shape in ZIMPOL data. We are currently working on a modified algorithm to account for the spatial features of the AO-corrected PSF. This is an on-going work and describing this method is beyond the scope of this Letter. This will be addressed in a dedicated forthcoming paper. We give very preliminary results in Fig. D.1 on two ZIMPOL acquisitions where the three moons are clearly visible.

We manually pinned strong hints of signal for the three moons in Fig. D.1. These data are temporally too far from the 2014 acquisitions to be added to the orbital fit of S3 performed with Genoid. We present them to further support the discovery of S3. The distance of the moon from Elektraat the different epochs is consistent with the orbital parameters given in Table 1 and discussed in Section 5.

In addition, we would like to mention here that for the 2016 epoch, the orbit planes of the moons are viewed edge-on. The angle between the orbits (adjusted on the 2014 observations) of S1and S2 and the orbit of S3 is given in Table C.4 and is 38° ± 19°. The highlighted position in Fig. D.1 matches the geometric projection of such an inclined orbit for S3. This suggests that this feature in the data could indeed be S3. More careful data analyses are needed to confirm this suspicion, but this is beyond the scope of this Letter. Indeed, as mentioned above, the data quality at this epoch is poor.

Appendix E: Astrophotometric measurements

The tables in this appendix gather the astrophotometry fit for the three moons of Elektra. In each table, x and y are the Cartesian positions of the moon relative to the photocentre of Elektraand ρ is the moon angular separation. Furetherore, δm is the moon magnitude relative to the primary, and D is the estimated moon diameter. The uncertainties on the positions are given on the top line of the tables for each date.

[6] https://www.aanda.org/10.1051/0004-6361/202142623/olm

Table E.1. Astrophotometry fit for S1 – S/2003 (130) 1.

9 Dec. 2014 (Julian date)	$x \pm 4.3$ (mas)	$y \pm 4.3$ (mas)	$\rho \pm 4.3$ (mas)	$\delta m \pm 0.20$	D (km)
2457000.56407	298.0	567.0	640	7.52	6.24
2457000.56446	297.0	567.0	640	7.56	6.12
2457000.56485	297.0	567.0	639	7.62	5.95
2457000.56525	296.0	566.0	639	7.60	6.01
2457000.56564	295.0	566.0	639	7.66	5.85
2457000.56609	295.0	566.0	639	7.65	5.87
2457000.56648	294.0	566.0	638	7.65	5.87
2457000.56688	294.0	566.0	638	7.66	5.85
2457000.56727	293.0	566.0	638	7.67	5.82
2457000.56766	293.0	566.0	637	7.66	5.85
2457000.56814	292.0	566.0	637	7.66	5.85
2457000.56853	292.0	566.0	637	7.67	5.82
2457000.56893	291.0	566.0	637	7.64	5.90
2457000.56932	291.0	566.0	636	7.66	5.85
2457000.56971	290.0	566.0	636	7.68	5.79
2457000.57016	290.0	566.0	636	7.65	5.87
2457000.57056	289.0	566.0	635	7.66	5.85
2457000.57095	288.0	566.0	635	7.68	5.79
2457000.57134	288.0	566.0	635	7.66	5.85
2457000.57174	287.0	566.0	635	7.65	5.87
2457000.57219	287.0	566.0	634	7.67	5.82
2457000.57258	286.0	566.0	634	7.63	5.93
2457000.57297	286.0	566.0	634	7.63	5.93
2457000.57337	285.0	565.0	633	7.63	5.93
2457000.57376	285.0	565.0	633	7.59	6.04
2457000.57422	284.0	565.0	633	7.57	6.09
2457000.57461	284.0	565.0	632	7.66	5.85
2457000.57500	283.0	565.0	632	7.61	5.98
2457000.57540	283.0	565.0	632	7.59	6.04
2457000.57579	282.0	565.0	632	7.60	6.01
2457000.57624	281.0	565.0	631	7.59	6.04
2457000.57663	281.0	565.0	631	7.60	6.01
2457000.57703	280.0	565.0	631	7.60	6.01
2457000.57742	280.0	565.0	630	7.59	6.04
2457000.57781	279.0	565.0	630	7.55	6.15
2457000.57826	279.0	565.0	630	7.59	6.04
2457000.57865	278.0	565.0	630	7.56	6.12
2457000.57904	278.0	565.0	629	7.58	6.07
2457000.57944	277.0	565.0	629	7.58	6.07
2457000.57983	277.0	565.0	629	7.56	6.12
2457000.58029	276.0	564.0	628	7.58	6.07
2457000.58068	276.0	564.0	628	7.53	6.21
2457000.58107	275.0	564.0	628	7.56	6.12
2457000.58147	275.0	564.0	628	7.55	6.15
2457000.58186	274.0	564.0	627	7.55	6.15
2457000.58232	274.0	564.0	627	7.58	6.07
2457000.58271	273.0	564.0	627	7.53	6.21
2457000.58310	272.0	564.0	626	7.54	6.18
2457000.58350	272.0	564.0	626	7.51	6.26
2457000.58389	271.0	564.0	626	7.54	6.18

Table E.1. continued.

30 Dec. 2014 (Julian date)	$x \pm 4.4$ (mas)	$y \pm 4.4$ (mas)	$\rho \pm 4.4$ (mas)	$\delta m \pm 0.20$	D (km)
2457021.54396	473.0	472.0	668	7.52	6.24
2457021.54435	473.0	472.0	668	7.49	6.32
2457021.54475	472.0	472.0	667	7.50	6.29
2457021.54514	471.0	472.0	667	7.52	6.24
2457021.54553	470.0	472.0	666	7.53	6.21
2457021.54592	470.0	472.0	666	7.49	6.32
2457021.54632	469.0	472.0	665	7.49	6.32
2457021.54671	468.0	472.0	665	7.51	6.26
2457021.54710	467.0	472.0	664	7.53	6.21
2457021.54749	467.0	472.0	664	7.52	6.24
2457021.55448	466.0	472.0	663	7.52	6.24
2457021.55488	465.0	472.0	663	7.49	6.32
2457021.55527	464.0	472.0	662	7.54	6.18
2457021.55566	464.0	473.0	662	7.52	6.24
2457021.55605	463.0	473.0	661	7.51	6.26
2457021.55645	462.0	473.0	661	7.47	6.38
2457021.55684	461.0	473.0	660	7.48	6.35
2457021.55723	460.0	473.0	660	7.53	6.21
2457021.55762	460.0	473.0	660	7.44	6.47
2457021.55802	459.0	473.0	659	7.48	6.35
2457021.56081	458.0	473.0	659	7.51	6.26
2457021.56120	457.0	473.0	658	7.48	6.35
2457021.56159	457.0	473.0	658	7.49	6.32
2457021.56198	456.0	473.0	657	7.44	6.47
2457021.56238	455.0	473.0	657	7.51	6.26
2457021.56277	454.0	473.0	656	7.48	6.35
2457021.56316	454.0	473.0	656	7.50	6.29
2457021.56355	453.0	473.0	655	7.46	6.41
2457021.56395	452.0	473.0	655	7.48	6.35
2457021.56434	451.0	473.0	654	7.51	6.26
2457021.56709	451.0	474.0	654	7.54	6.18
2457021.56748	450.0	474.0	653	7.52	6.24
2457021.56788	449.0	474.0	653	7.49	6.32
2457021.56827	448.0	474.0	652	7.48	6.35
2457021.56866	448.0	474.0	652	7.49	6.32
2457021.56905	447.0	474.0	651	7.48	6.35
2457021.56945	446.0	474.0	651	7.51	6.26
2457021.56984	445.0	474.0	650	7.50	6.29
2457021.57023	445.0	474.0	650	7.48	6.35
2457021.57062	444.0	474.0	649	7.48	6.35
2457021.68937	309.0	478.0	569	7.71	5.71
2457021.68976	309.0	478.0	569	7.66	5.85
2457021.69016	308.0	478.0	568	7.58	6.07
2457021.69055	307.0	478.0	568	7.59	6.04
2457021.69094	307.0	478.0	568	7.53	6.21
2457021.69133	306.0	478.0	567	7.57	6.09
2457021.69173	305.0	477.0	567	7.57	6.09
2457021.69212	305.0	477.0	566	7.58	6.07
2457021.69251	304.0	477.0	566	7.57	6.09
2457021.69290	303.0	477.0	566	7.46	6.41
2457021.69563	303.0	477.0	565	7.56	6.12
2457021.69602	302.0	477.0	565	7.53	6.21

Table E.1. continued.

2457021.69642	301.0	477.0	564	7.52	6.24
2457021.69681	301.0	477.0	564	7.46	6.41
2457021.69720	300.0	477.0	564	7.52	6.24
2457021.69759	300.0	477.0	563	7.49	6.32
2457021.69799	299.0	477.0	563	7.44	6.47
2457021.69838	298.0	477.0	562	7.48	6.35
2457021.69877	298.0	477.0	562	7.46	6.41
2457021.69916	297.0	477.0	561	7.73	5.66
2457021.70188	296.0	476.0	561	7.66	5.85
2457021.70228	296.0	476.0	561	7.58	6.07
2457021.70267	295.0	476.0	560	7.60	6.01
2457021.70306	294.0	476.0	560	7.53	6.21
2457021.70345	294.0	476.0	559	7.57	6.09
2457021.70385	293.0	476.0	559	7.57	6.09
2457021.70424	292.0	476.0	559	7.56	6.12
2457021.70463	292.0	476.0	558	7.57	6.09
2457021.70502	291.0	476.0	558	7.49	6.32
2457021.70541	291.0	476.0	557	7.56	6.12
31 Dec. 2014 (Julian date)	$x \pm 4.4$ (mas)	$y \pm 4.4$ (mas)	$\rho \pm 4.4$ (mas)	$\delta m \pm 0.20$	D (km)
2457022.65498	-688.0	99.0	695	7.67	5.82
2457022.65537	-688.0	99.0	695	7.72	5.69
2457022.65576	-688.0	98.0	695	7.67	5.82
2457022.65615	-689.0	98.0	696	7.71	5.71
2457022.65655	-689.0	98.0	696	7.71	5.71
2457022.65694	-689.0	97.0	696	7.70	5.74
2457022.65733	-689.0	97.0	696	7.74	5.63
2457022.65772	-690.0	96.0	696	7.74	5.63
2457022.65812	-690.0	96.0	697	7.65	5.87
2457022.65851	-690.0	95.0	697	7.73	5.66
2457022.66125	-691.0	95.0	697	7.66	5.85
2457022.66164	-691.0	94.0	697	7.58	6.07
2457022.66204	-691.0	94.0	698	7.60	6.01
2457022.66243	-692.0	94.0	698	7.53	6.21
2457022.66282	-692.0	93.0	698	7.57	6.09
2457022.66321	-692.0	93.0	698	7.57	6.09
2457022.66361	-693.0	92.0	699	7.58	6.07
2457022.66400	-693.0	92.0	699	7.57	6.09
2457022.66439	-693.0	91.0	699	7.49	6.32
2457022.66478	-693.0	91.0	699	7.56	6.12
2457022.66750	-694.0	90.0	700	7.53	6.21
2457022.66789	-694.0	90.0	700	7.52	6.24
2457022.66828	-694.0	89.0	700	7.46	6.41
2457022.66867	-695.0	89.0	700	7.52	6.24
2457022.66907	-695.0	88.0	701	7.49	6.32
2457022.66946	-695.0	88.0	701	7.42	6.53
2457022.66985	-696.0	88.0	701	7.48	6.35
2457022.67024	-696.0	87.0	701	7.46	6.41
2457022.67064	-696.0	87.0	702	7.48	6.35
2457022.67103	-696.0	86.0	702	7.48	6.35

Table E.2. Astrophotometry fit for S2 – S/2014 (130) 1.

9 Dec. 2014 (Julian date)	$x \pm 4.3$ (mas)	$y \pm 4.3$ (mas)	$\rho \pm 4.3$ (mas)	$\delta m \pm 0.30$	D (km)
2457000.56407	356.3	8.7	356	9.76	2.22
2457000.56446	356.5	9.2	357	9.82	2.16
2457000.56485	356.6	9.8	357	9.98	2.01
2457000.56525	356.8	10.3	357	9.80	2.18
2457000.56564	357.0	10.9	357	10.12	1.88
2457000.56609	357.2	11.4	357	10.00	1.99
2457000.56648	357.4	12.0	358	10.03	1.96
2457000.56688	357.6	12.5	358	10.32	1.72
2457000.56727	357.8	13.1	358	10.07	1.93
2457000.56766	358.0	13.6	358	9.97	2.02
2457000.56814	358.2	14.2	359	10.06	1.94
2457000.56853	358.4	14.8	359	10.02	1.97
2457000.56893	358.6	15.3	359	9.96	2.03
2457000.56932	358.7	15.9	359	9.86	2.12
2457000.56971	358.9	16.4	359	9.93	2.06
2457000.57016	359.1	17.0	360	9.97	2.02
2457000.57056	359.3	17.5	360	10.12	1.88
2457000.57095	359.5	18.1	360	10.06	1.94
2457000.57134	359.7	18.6	360	9.99	2.00
2457000.57174	359.8	19.2	360	10.06	1.94
2457000.57219	360.0	19.8	361	9.96	2.03
2457000.57258	360.2	20.3	361	10.24	1.78
2457000.57297	360.4	20.9	361	10.03	1.96
2457000.57337	360.5	21.4	361	10.10	1.90
2457000.57376	360.7	22.0	361	10.10	1.90
2457000.57422	360.9	22.6	362	10.03	1.96
2457000.57461	361.1	23.1	362	10.21	1.81
2457000.57500	361.2	23.7	362	9.98	2.01
2457000.57540	361.4	24.2	362	9.93	2.06
2457000.57579	361.6	24.8	362	10.05	1.94
2457000.57624	361.8	25.4	363	10.17	1.84
2457000.57663	361.9	25.9	363	10.01	1.98
2457000.57703	362.1	26.5	363	9.95	2.04
2457000.57742	362.3	27.1	363	10.23	1.79
2457000.57781	362.4	27.6	364	10.07	1.93
2457000.57826	362.6	28.2	364	10.13	1.87
2457000.57865	362.8	28.8	364	10.10	1.90
2457000.57904	362.9	29.3	364	10.12	1.88
2457000.57944	363.1	29.9	364	9.97	2.02
2457000.57983	363.3	30.5	365	10.00	1.99
2457000.58029	363.4	31.1	365	9.88	2.10
2457000.58068	363.6	31.6	365	10.00	1.99
2457000.58107	363.8	32.2	365	9.96	2.03
2457000.58147	363.9	32.8	365	9.77	2.21
2457000.58186	364.1	33.3	366	10.01	1.98
2457000.58232	364.2	33.9	366	10.02	1.97
2457000.58271	364.4	34.5	366	10.17	1.84
2457000.58310	364.5	35.1	366	10.03	1.96
2457000.58350	364.7	35.6	366	10.11	1.89
2457000.58389	364.8	36.2	367	9.94	2.05

Table E.2. continued.

30 Dec. 2014 (Julian date)	$x \pm 4.5$ (mas)	$y \pm 4.5$ (mas)	$\rho \pm 4.5$ (mas)	$\delta m \pm 0.40$	D (km)
2457021.54396	-317.9	-112.2	337	9.82	2.16
2457021.54435	-317.5	-113.1	337	10.31	1.73
2457021.54475	-317.2	-113.9	337	10.24	1.78
2457021.54514	-316.8	-114.8	337	10.06	1.94
2457021.54553	-316.4	-115.6	337	10.06	1.94
2457021.54592	-316.1	-116.5	337	10.17	1.84
2457021.54632	-315.7	-117.3	337	10.17	1.84
2457021.54671	-315.3	-118.1	337	10.09	1.91
2457021.54710	-315.0	-119.0	337	10.06	1.94
2457021.54749	-314.6	-119.8	337	10.15	1.86
2457021.55448	-314.2	-120.6	337	10.36	1.69
2457021.55488	-313.8	-121.5	337	10.07	1.93
2457021.55527	-313.4	-122.3	336	10.38	1.67
2457021.55566	-313.1	-123.1	336	9.99	2.00
2457021.55605	-312.7	-124.0	336	10.07	1.93
2457021.55645	-312.3	-124.8	336	10.14	1.87
2457021.55684	-311.9	-125.6	336	9.94	2.05
2457021.55723	-311.5	-126.4	336	10.35	1.69
2457021.55762	-311.1	-127.3	336	10.24	1.78
2457021.55802	-310.7	-128.1	336	10.19	1.82
2457021.56081	-310.3	-128.9	336	10.14	1.87
2457021.56120	-309.9	-129.7	336	10.38	1.67
2457021.56159	-309.5	-130.5	336	10.04	1.95
2457021.56198	-309.1	-131.4	336	10.13	1.87
2457021.56238	-308.7	-132.2	336	10.10	1.90
2457021.56277	-308.3	-133.0	336	10.31	1.73
2457021.56316	-307.9	-133.8	336	10.04	1.95
2457021.56355	-307.4	-134.6	336	10.13	1.87
2457021.56395	-307.0	-135.4	336	9.89	2.09
2457021.56434	-306.6	-136.2	336	9.93	2.06
2457021.56709	-306.2	-137.1	335	9.86	2.12
2457021.56748	-305.8	-137.9	335	10.03	1.96
2457021.56788	-305.3	-138.7	335	9.72	2.26
2457021.56827	-304.9	-139.5	335	9.65	2.34
2457021.56866	-304.5	-140.3	335	9.64	2.35
2457021.56905	-304.1	-141.1	335	9.62	2.37
2457021.56945	-303.6	-141.9	335	9.84	2.14
2457021.56984	-303.2	-142.7	335	9.77	2.21
2457021.57023	-302.7	-143.5	335	9.77	2.21
2457021.57062	-302.3	-144.3	335	9.79	2.19
31 Dec. 2014 (Julian date)	$x \pm 5.2$ (mas)	$y \pm 5.2$ (mas)	$\rho \pm 5.2$ (mas)	$\delta m \pm 0.40$	D (km)
2457022.65498	-314.1	-37.8	316	10.44	1.62
2457022.65537	-314.2	-38.3	317	10.43	1.63
2457022.65576	-314.4	-38.7	317	10.39	1.66

Table E.2. continued.

2457022.65615	-314.6	-39.2	317	10.33	1.71
2457022.65655	-314.8	-39.7	317	10.19	1.82
2457022.65694	-315.0	-40.2	318	10.00	1.99
2457022.65733	-315.2	-40.7	318	10.26	1.77
2457022.65772	-315.3	-41.2	318	10.11	1.89
2457022.65812	-315.5	-41.6	318	10.64	1.48
2457022.65851	-315.7	-42.1	318	10.13	1.87
2457022.66125	-315.9	-42.6	319	9.86	2.12
2457022.66164	-316.0	-43.1	319	9.95	2.04
2457022.66204	-316.2	-43.6	319	9.96	2.03
2457022.66243	-316.4	-44.1	319	9.85	2.13
2457022.66282	-316.6	-44.6	320	10.09	1.91
2457022.66321	-316.7	-45.1	320	10.05	1.94
2457022.66361	-316.9	-45.6	320	10.02	1.97
2457022.66400	-317.1	-46.0	320	9.93	2.06
2457022.66439	-317.3	-46.5	321	9.95	2.04
2457022.66478	-317.4	-47.0	321	10.02	1.97
2457022.66750	-317.6	-47.5	321	10.17	1.84
2457022.66789	-317.8	-48.0	321	10.47	1.60
2457022.66828	-317.9	-48.5	322	9.95	2.04
2457022.66867	-318.1	-49.0	322	10.49	1.59
2457022.66907	-318.3	-49.5	322	9.94	2.05
2457022.66946	-318.4	-50.0	322	10.03	1.96
2457022.66985	-318.6	-50.5	323	10.11	1.89
2457022.67024	-318.8	-51.0	323	10.05	1.94
2457022.67064	-318.9	-51.5	323	10.27	1.76
2457022.67103	-319.1	-52.0	323	9.71	2.27

Table E.3. Astrophotometry fit for S3 – S/2014 (130) 2.

9 Dec. 2014 (Julian date)	$x \pm 6.0$ (mas)	$y \pm 6.0$ (mas)	$\rho \pm 6.0$ (mas)	$\delta m \pm 0.50$	D (km)
2457000.56407	55.8	-253.4	259	10.26	1.77
2457000.56446	56.4	-253.2	259	10.45	1.62
2457000.56485	57.0	-253.0	259	10.69	1.45
2457000.56525	57.6	-252.9	259	10.39	1.66
2457000.56564	58.2	-252.7	259	10.66	1.47
2457000.56609	58.8	-252.5	259	10.56	1.54
2457000.56648	59.4	-252.3	259	10.36	1.69
2457000.56688	60.0	-252.1	259	10.43	1.63
2457000.56727	60.7	-251.9	259	10.60	1.51
2457000.56766	61.3	-251.7	259	10.41	1.65
2457000.56814	61.8	-251.5	259	10.54	1.55
2457000.56853	62.4	-251.3	259	10.65	1.48
2457000.56893	63.0	-251.1	259	10.39	1.66
2457000.56932	63.6	-250.9	259	10.39	1.66
2457000.56971	64.2	-250.7	259	9.80	2.18
2457000.57016	64.8	-250.5	259	10.64	1.48
2457000.57056	65.4	-250.3	259	10.54	1.55
2457000.57095	66.0	-250.1	259	10.76	1.40
2457000.57134	66.6	-249.9	259	10.64	1.48
2457000.57174	67.2	-249.7	259	10.75	1.41
2457000.57219	67.8	-249.5	259	10.41	1.65
2457000.57258	68.4	-249.2	258	10.56	1.54
2457000.57297	69.0	-249.0	258	10.27	1.76
2457000.57337	69.6	-248.8	258	10.52	1.57
2457000.57376	70.2	-248.6	258	10.61	1.50
2457000.57422	70.8	-248.4	258	10.43	1.63
2457000.57461	71.4	-248.2	258	10.48	1.60
2457000.57500	72.0	-247.9	258	10.40	1.66
2457000.57540	72.5	-247.7	258	10.37	1.68
2457000.57579	73.1	-247.5	258	10.46	1.61
2457000.57624	73.7	-247.3	258	10.51	1.57
2457000.57663	74.3	-247.0	258	10.28	1.75
2457000.57703	74.9	-246.8	258	10.56	1.54
2457000.57742	75.5	-246.6	258	10.47	1.60
2457000.57781	76.1	-246.3	258	10.33	1.71
2457000.57826	76.6	-246.1	258	10.64	1.48
2457000.57865	77.2	-245.9	258	10.39	1.66
2457000.57904	77.8	-245.6	258	10.67	1.46
2457000.57944	78.4	-245.4	258	10.54	1.55
2457000.57983	79.0	-245.2	258	10.41	1.65
2457000.58029	79.5	-244.9	258	10.20	1.81
2457000.58068	80.1	-244.7	257	10.49	1.59
2457000.58107	80.7	-244.5	257	10.76	1.40
2457000.58147	81.3	-244.2	257	11.07	1.22
2457000.58186	81.9	-244.0	257	10.59	1.52
2457000.58232	82.4	-243.7	257	10.61	1.50
2457000.58271	83.0	-243.5	257	10.48	1.60
2457000.58310	83.6	-243.2	257	10.86	1.34
2457000.58350	84.2	-243.0	257	10.59	1.52
2457000.58389	84.7	-242.7	257	10.68	1.45

Table E.3. continued.

30 Dec. 2014 (Julian date)	$x \pm 7.1$ (mas)	$y \pm 7.1$ (mas)	$\rho \pm 7.1$ (mas)	$\delta m \pm 0.50$	D (km)
2457021.54396	-70.7	-233.3	244	10.51	1.57
2457021.54435	-69.4	-232.9	243	10.60	1.51
2457021.54475	-68.1	-232.5	242	9.89	2.09
2457021.54514	-66.8	-232.1	242	11.25	1.12
2457021.54553	-65.5	-231.7	241	10.47	1.60
2457021.54592	-64.2	-231.3	240	10.39	1.66
2457021.54632	-62.9	-230.8	239	10.89	1.32
2457021.54671	-61.7	-230.4	239	10.66	1.47
2457021.54710	-60.4	-230.0	238	10.44	1.62
2457021.54749	-59.1	-229.5	237	10.50	1.58
2457021.55448	-57.9	-229.1	236	9.95	2.04
2457021.55488	-56.6	-228.6	236	10.20	1.81
2457021.55527	-55.4	-228.2	235	10.17	1.84
2457021.55566	-54.1	-227.7	234	10.30	1.73
2457021.55605	-52.9	-227.2	233	10.32	1.72
2457021.55645	-51.6	-226.7	233	10.26	1.77
2457021.55684	-50.4	-226.2	232	10.35	1.69
2457021.55723	-49.2	-225.7	231	10.43	1.63
2457021.55762	-48.0	-225.2	230	10.23	1.79
2457021.55802	-46.8	-224.7	230	9.98	2.01
2457021.56081	-45.6	-224.2	229	10.26	1.77
2457021.56120	-44.4	-223.7	228	9.79	2.19
2457021.56159	-43.2	-223.2	227	10.08	1.92
2457021.56198	-42.0	-222.6	227	9.99	2.00
2457021.56238	-40.8	-222.1	226	10.29	1.74
2457021.56277	-39.6	-221.5	225	9.71	2.27
2457021.56316	-38.5	-221.0	224	9.96	2.03
2457021.56355	-37.3	-220.4	224	10.23	1.79
2457021.56395	-36.1	-219.9	223	10.32	1.72
2457021.56434	-35.0	-219.3	222	9.99	2.00
2457021.56709	-33.8	-218.7	221	10.24	1.78
2457021.56748	-32.7	-218.1	221	9.98	2.01
2457021.56788	-31.6	-217.5	220	9.41	2.61
2457021.56827	-30.4	-216.9	219	9.56	2.44
2457021.56866	-29.3	-216.3	218	9.67	2.32
2457021.56905	-28.2	-215.7	218	10.30	1.73
2457021.56945	-27.1	-215.1	217	10.02	1.97
2457021.56984	-26.0	-214.5	216	9.98	2.01
2457021.57023	-24.9	-213.9	215	9.94	2.05
2457021.57062	-23.8	-213.3	215	10.02	1.97
31 Dec. 2014 (Julian date)	$x \pm 6.2$ (mas)	$y \pm 6.2$ (mas)	$\rho \pm 6.2$ (mas)	$\delta m \pm 0.50$	D (km)
2457022.65498	-312.8	14.0	313	11.10	1.20
2457022.65537	-313.2	13.8	314	10.67	1.46
2457022.65576	-313.6	13.6	314	10.21	1.81
2457022.65615	-314.0	13.4	314	10.74	1.42
2457022.65655	-314.4	13.2	315	10.05	1.94
2457022.65694	-314.8	13.0	315	10.37	1.68
2457022.65733	-315.2	12.7	316	10.53	1.56
2457022.65772	-315.7	12.5	316	10.15	1.86

Table E.3. continued.

2457022.65812	-316.1	12.3	316	10.85	1.35
2457022.65851	-316.5	12.1	317	10.83	1.36
2457022.66125	-316.9	11.9	317	10.36	1.69
2457022.66164	-317.3	11.7	318	10.24	1.78
2457022.66204	-317.7	11.4	318	10.36	1.69
2457022.66243	-318.1	11.2	318	10.34	1.70
2457022.66282	-318.5	11.0	319	10.15	1.86
2457022.66321	-318.9	10.8	319	10.13	1.87
2457022.66361	-319.3	10.6	320	10.28	1.75
2457022.66400	-319.7	10.3	320	10.17	1.84
2457022.66439	-320.1	10.1	320	10.38	1.67
2457022.66478	-320.5	9.9	321	10.45	1.62
2457022.66750	-321.0	9.7	321	10.62	1.50
2457022.66789	-321.4	9.4	322	10.30	1.73
2457022.66828	-321.8	9.2	322	10.20	1.81
2457022.66867	-322.2	9.0	322	10.28	1.75
2457022.66907	-322.6	8.8	323	10.22	1.80
2457022.66946	-323.0	8.5	323	10.31	1.73
2457022.66985	-323.4	8.3	324	10.98	1.27
2457022.67024	-323.8	8.1	324	11.55	0.97
2457022.67064	-324.2	7.9	324	10.56	1.54
2457022.67103	-324.6	7.6	325	10.56	1.54